The Astrophysical Journal, 931:88 (19pp), 2022 June 1 https://doi.org/10.3847/1538-4357/ac6873

Redshift Estimation and Constraints on Intergalactic and Interstellar Media from Dispersion and Scattering of Fast Radio Bursts

J. M. Cordes, Stella Koch Ocker, and Shami Chatterjee

Department of Astronomy and Cornell Center for Astrophysics and Planetary Science, Cornell University, Ithaca, NY 14853, USA; jmc33@cornell.edu

Received 2021 August 3; revised 2022 April 5; accepted 2022 April 18; published 2022 May 27

Abstract

A sample of 14 FRBs with measured redshifts and scattering times is used to assess contributions to dispersion and scattering from the intergalactic medium (IGM), galaxy halos, and the disks of host galaxies. The IGM and galaxy halos contribute significantly to dispersion measures (DMs) but evidently not to scattering, which is then dominated by host galaxies. This enables the usage of scattering times for estimating DM contributions from host galaxies and also for a combined scattering–dispersion redshift estimator. Redshift estimation is calibrated using the scattering of Galactic pulsars after taking into account different scattering geometries for Galactic and intergalactic lines of sight. The DM-only estimator has a bias of ∼0.1 and rms error of ∼0.15 in the redshift estimate for an assumed ad hoc value of 50 pc cm^{-3} for the host galaxy's DM contribution. The combined redshift estimator shows less bias by a factor of 4 to 10 and a 20%–40% smaller rms error. We find that values for the baryonic fraction of the ionized IGM $f_{\rm igm} \simeq 0.85 \pm 0.05$ optimize redshift estimation using dispersion and scattering. Our study suggests that 2 of the 14 candidate galaxy associations (FRB 20190523A and FRB 20190611B) should be reconsidered.

Unified Astronomy Thesaurus concepts: Radio pulsars (1353); Radio transient sources (2008); Radio bursts (1339); Intergalactic medium (813); Interstellar scattering (854); Interstellar medium (847); Baryon density (139); Interstellar plasma (851)

1. Introduction

Of the hundreds of distinct sources of fast radio bursts (FRBs) that have been recognized to date, there are only 14 published cases with associated galaxies and redshifts. By contrast, the dispersion measure (DM), the path-integrated electron density, is necessarily measured concomitantly with burst detections, and in many cases, measurements or upper limits are also obtained on characteristic scattering times from multipath propagation.

Because FRB distances are necessary for understanding both the energetics and the size of the FRB source population, significant efforts now aim to make subarcsecond localizations that aid subsequent spectroscopic observations to determine redshifts. It will be some time before these efforts yield large numbers of redshifts. In the meantime, coarser redshift estimates can be made using DM values combined with electron-density models for the Milky Way (MW) and the intergalactic medium (IGM) and assumptions about contributions from host galaxies. Indeed, a recent study has shown a trend for larger DM with increasing redshifts, as expected, but with significant scatter (Macquart et al. 2020). Some of this scatter is from cosmic variance in the electron density in the IGM but the sizable range of DM contributions from host galaxies also contributes. In this paper, we develop and assess a redshift estimator that uses scattering measurements in tandem with DM values to better constrain host-galaxy DMs and thus tighten constraints on redshifts. Balmer-line measurements also contribute to this analysis (Bassa et al. 2017; Tendulkar et al. 2017) and will play an increasingly important role in the future as more FRB sources are localized (e.g., Simard & Ravi 2021). While nearing completion of this paper, FRB 20190520B with a large total DM was found to be associated with a low-redshift galaxy (Niu et al. 2021). This object corroborates the main results of this paper, but a detailed analysis is deferred to another paper (Ocker et al. 2022a).

Section 2 discusses contributions to DM and presents posterior probability density functions (PDFs) for host-galaxy DMs for the 14 objects with redshifts of associated galaxies (which are tentative in a few cases).

Section 3 assesses contributions to scattering in the context of a parameterized cloudlet model that is calibrated against the scattering of Galactic pulsars. The section presents alternative geometries for FRB scattering under the assumption that IGM and galaxy halos do not contribute significantly to measured scattering.

Section 4 presents a combined analysis of dispersion and scattering for the nine objects with scattering and redshift measurements. It includes estimates of the $\widetilde{F}$ parameter, which is a measure of the scattering strength in the cloudlet model.

Section 5 considers redshift estimation using only DMs versus the usage of scattering in tandem with dispersion. It presents a criterion for when scattering can usefully constrain the redshift and presents results that also constrain the baryonic fraction of the ionized IGM.

Section 6 presents a summary and our conclusions.

The Appendix presents details of the cloudlet-scattering model.

Naming convention: In the text and in Tables 1–3 we use the full FRB name (e.g., FRB 20121102A) given by the Transient Name Server.[1] Most figure labeling uses short labels (e.g.,

---

[1] https://www.wis-tns.org

Table 1
FRB Scattering and Redshift Sample

FRB	l	b	DM	$\mathrm{DM_{NE2001}}$	W	z_{h}	τ	σ_-	σ_+	ν_τ	References	
	(degrees)		(pc $\mathrm{cm^{-3}}$)	(pc $\mathrm{cm^{-3}}$)	(ms)	(ms)	(ms)	(ms)	(GHz)	z_{h}[a]	τ[b]	
(1)	(2)	(3)	(4)	(5)	(6)	(7)	(8)	(9)	(10)	(11)	(12)	(13)
20121102A	174.9	−0.2	557	188	3.0	0.193	<9.6	⋯	⋯	0.50	1	1
20180916B[c]	129.7	3.7	349	199	0.87	0.034	<1.7	⋯	⋯	0.35	2	2
20180924A	0.74	−49.4	361	40	1.30	0.321	0.68	0.03	0.030	1.27	3	3
20181112A	−17.4	−47.7	589	42	2.1	0.475	0.021	0.001	0.001	1.30	4	4
20190102B	−47.4	−33.5	364	57	1.7	0.291	0.041	0.003	0.002	1.27	5	3
20190523A	117.0	44.0	761	37	0.42	0.660	1.4	0.2	0.20	1.0	6	5
20190608B	53.2	−48.5	339	37	6.0	0.118	3.3	0.2	0.20	1.27	5	3
20190611B[d]	−47.1	−33.3	321	58	2 .0	0.378	0.18	0.02	0.020	1.30	5,7	3
20190711A	−49.1	−33.9	593	56	6.5	0.522	<1.12	⋯	⋯	1.30	5	6
20190714A	−71.1	48.7	504	39	2.0	0.2365	<2	⋯	⋯	1.27	7	7[e]
20191001A	−17.3	−44.0	507	44	10	0.234	3.3	0.2	0.2	0.824	7	8
20200430A	17.1	52.5	380	27	15.	0.16	10	5	5	0.865	7	9[e]
20200120E[f]	142.2	41.22	88	41	0.1	(3.6 Mpc)	<30 ns	⋯	⋯	1.40	⋯	10
20201124A	177.8	−8.52	414	140	3.2	0.098	5.6	3	3	0.865	8,9	11

Notes.

[a] References for z_{h}: (1) Tendulkar et al. (2017), (2) Marcote et al. (2020); (3) Bannister et al. (2019); (4) Prochaska et al. (2019); (5) Macquart et al. (2020); (6) Ravi et al. (2019); (7) Heintz et al. (2020); (8) Kilpatrick et al. (2021); (9) Ravi et al. (2022).

[b] References for τ: (1) Josephy et al. (2019); (2) Chawla et al. (2020); (3) Day et al. (2020); (4) Cho et al. (2020); (5) Ravi et al. (2019); (6) Qiu et al. (2020); (7) Bhandari et al. (2019); (8) Bhandari et al. (2020); (9) Kumar et al. (2020); (10) Nimmo et al. (2022); (11) Kumar et al. (2021).

[c] Pulse broadening has been measured at 0.15 GHz (Pastor-Marazuela et al. 2021) from Galactic scattering; the upper bound for this object refers to any extragalactic scattering.

[d] The association of this FRB with the candidate galaxy at the redshift z_{h} in column 7 is stated to be tentative (Macquart et al. 2020).

[e] The estimate for τ is based on the dynamic spectrum linked to the quoted reference.

[f] FRB source is associated with a globular cluster in the M81 system (Kirsten et al. 2022) at a distance of 3.6 Mpc with a formally negative redshift. Measured scintillations are Galactic in origin and correspond to a scattering time of ∼27 ns (Nimmo et al. 2022). Extragalactic scattering is not evident so we take 30 ns as an upper limit.

121102), which is unambiguous for the sample we analyze and discuss.

2. Dispersion Measure Inventory

The objects we analyze are listed in Table 1 with columns (1) FRB name; (2)–(3) Galactic coordinates l, b; (4) DM; (5) NE2001 estimate for the MW contribution to DM (sans an MW halo contribution); (6) burst width—for the repeating FRBs 20121102A and 20180916B, this is a typical value; (7) τ (measurement or limit); (9)–(10) + and − rms errors in τ; (11) radio frequency for the τ entries; (12) reference for z_{h}; and (13) reference for τ.

We note that determinations of τ need to be used with caution because some are made on bursts with low signal-to-noise ratios or that appear in a narrow frequency band. Another problem is the frequency drift ("sad trombone") phenomenon seen in many bursts (e.g., CHIME/FRB Collaboration et al. 2019; Hessels et al. 2019; Cho et al. 2020; Fonseca et al. 2020) that can produce asymmetries in wide-bandwidth burst profiles that are similar to those expected from scattering. We assume that all scattering measurements in Table 1 are unaffected by frequency drifts or other effects that can masquerade as scattering asymmetries.

The $\mathrm{DM} = \int ds\, n_{\mathrm{e}}(s)$, expressed in standard units of pc $\mathrm{cm^{-3}}$, is estimated from chromatic arrival times and receives contributions from all nonrelativistic plasmas along the line of sight (LoS). While we exclude the small contributions originating within the solar system we include all others between the solar system and an FRB source.

As is usual in the FRB literature, we write the measured DM for a source at redshift z_{h} as the sum,

$$\mathrm{DM} = \mathrm{DM_{mw}} + \mathrm{DM_{igm}}(z_{\mathrm{h}}) + \frac{\mathrm{DM_{igh}}}{1 + z_{\mathrm{igh}}} + \frac{\mathrm{DM_h}}{1 + z_{\mathrm{h}}}, \qquad (1)$$

that includes components from the Milky Way (mw), the intergalactic medium (igm), a possible intervening galaxy or halo (igh), and a host galaxy (h), including its halo. The MW term includes both the nonhalo ("disk") and halo components, $\mathrm{DM_{mw}} = \mathrm{DM_{mw,disk}} + \mathrm{DM_{mw,halo}}$, that are estimated separately because their phenomenology and characterization differ substantially. The IGM contribution displays cosmic variance indicative of the stochastic distribution of galaxy halos and requires a statistical dependence on redshift, z. The last two terms involve the reduction of the rest-frame DMs, $\mathrm{DM_{igh}}$ and $\mathrm{DM_h}$, by $1/(1+z)$ factors for the intervening and host galaxies. For simplicity, all possible contributions to $\mathrm{DM_h}$ (galaxy disk, halo, and circumsource region) are lumped together.

2.1. Milky Way Contribution

The "disk" contribution to DM from the MW is obtained by integrating the direction-dependent NE2001 model (Cordes & Lazio 2002) through the entire Galaxy to give $\mathrm{DM_{mw,disk}}(l, b)$. The NE2001 model actually comprises two disk components, spiral arms, and localized regions. The differences between the NE2001 model and the alternative YMW16 model (Yao et al. 2017) are negligible for FRBs at Galactic latitudes $\gtrsim 20°$ but NE2001 is more accurate for FRB 20121102A in the Galactic anticenter direction (Ocker et al. 2021). Also, the YMW16

Table 2
FRB DM Inventory and Redshift Estimates from the DM

FRB	DM	z_h	$\mathrm{DM_{mw}}$[a]		$\mathrm{DM_{igm}}$[b](f_{igm}= 0.85)			$\mathrm{DM_h}$[c](f_{igm}= 0.85)			$\hat{z}$(DM, f_{igm} = 0.85)		
	(pc cm^{-3})		(pc cm^{-3})		(pc cm^{-3})			(pc cm^{-3})					
(1)	(2)	(3)	(4)	(5)	(6)	(7)	(8)	(9)	(10)	(11)	(12)	(13)	(14)
20121102A	557	0.193	241	±27	152	−59	+97	215	−83	+69	0.373	−0.117	+0.125
20180916B	349	0.034	252	±28	24	−12	+36	82	−33	+33	0.103	−0.048	+0.066
20180924A	361	0.321	93	±17	268	−87	+129	99	−52	+67	0.319	−0.105	+0.113
20181112A	589	0.475	94	±17	411	−114	+159	206	−118	+128	0.571	−0.153	+0.158
20190102B	364	0.291	110	±17	240	−81	+122	100	−53	+64	0.302	−0.101	+0.110
20190523A	761	0.660	90	±16	585	−142	+188	261	−155	+178	0.762	−0.183	+0.188
20190608B	339	0.118	90	±16	87	−39	+72	190	−68	+45	0.297	−0.100	+0.108
20190611B	321	0.378	110	±17	320	−97	+141	58	−26	+43	0.253	−0.089	+0.099
20190711A	593	0.522	109	±17	455	−122	+167	171	−100	+123	0.559	−0.151	+0.157
20190714A	504	0.236	91	±16	191	−69	+109	289	−116	+83	0.481	−0.138	+0.143
20191001A	507	0.234	97	±17	188	−68	+109	287	−115	+82	0.477	−0.137	+0.143
20200430A	380	0.160	80	±16	123	−50	+87	217	−84	+58	0.356	−0.113	+0.120
FRB20200120E	88	⋯	93	±17	<1	⋯	⋯	13	−6	+7	⋯	⋯	⋯
20201124A	414	0.098	192	±23	71	−33	+64	172	−60	+44	0.305	−0.100	+0.107

Notes.

[a] $\mathrm{DM_{mw}}$ includes contributions from the disk using the NE2001 model and halo described in Section 2.1.

[b] $\mathrm{DM_{igm}}$ is calculated using the redshift z_h and the log-normal model of Section 2.2.

[c] $\mathrm{DM_h}$ values are in the frame of the host galaxy at redshift z_h and are calculated by integrating over the PDFs for $\mathrm{DM_{mw}}$ and $\mathrm{DM_{igm}}$ using Equation (6).

Table 3
FRB Host-galaxy Parameters and Redshift Estimates

FRB	DM (pc cm^{-3})	z_h	$\mathrm{DM_h}$ (pc cm^{-3})	$A_\tau \widetilde{F} G$ ((pc^2 km)$^{-1/3}$)	$\hat{z}$(DM, τ, narrow)			$\hat{z}$(DM, τ, wide)		
(1)	(2)	(3)	(4)	(5)	(6)	(7)	(8)	(9)	(10)	(11)
20121102A	557	0.193	215	<0.46	⋯	⋯	⋯	⋯	⋯	⋯
20180916B	349	0.034	82	<0.092	⋯	⋯	⋯	⋯	⋯	⋯
20180924A	361	0.321	99	8.7	0.128	−0.066	+0.080	0.216	−0.097	+0.106
20181112A	589	0.475	206	0.094	0.566	−0.147	+0.151	0.561	−0.159	+0.159
20190102B	364	0.291	100	0.48	0.290	−0.094	+0.101	0.292	−0.111	+0.113
20190523A	761	0.660	261	2.0	0.576	−0.147	+0.153	0.623	−0.206	+0.190
20190608B	339	0.118	190	7.0	0.027	−0.005	+0.009	0.111	−0.049	+0.075
20190611B	321	0.378	58	8.3	0.170	−0.067	+0.079	0.207	−0.092	+0.099
20190711A	593	0.522	171	<8.0	⋯	⋯	⋯	⋯	⋯	⋯
20190714A	504	0.236	289	<2.5	⋯	⋯	⋯	⋯	⋯	⋯
20191001A	507	0.234	287	0.72	0.298	−0.099	+0.109	0.356	−0.152	+0.143
20200430A	380	0.160	217	3.9	0.124	−0.075	+0.141	0.205	−0.108	+0.128
20200120E	88	⋯	13	<0.014	⋯	⋯	⋯	⋯	⋯	⋯
20201124A	414	0.098	172	3.9	0.109	−0.064	+0.117	0.165	−0.088	+0.109

model does not properly estimate scattering observables and thus cannot be used in our analysis of scattering.

For high-latitude LoSs, the spread in estimated values for $\mathrm{DM_{mw}}$ is several tens of pc cm^{-3}, primarily from uncertainties in the contribution from the Galactic halo. For the two low-latitude cases, FRB 20121102A and FRB 20180916B, the uncertainty in $\mathrm{DM_{mw}}$ could be substantially larger. However, for FRB 20121102A, the measured redshift and the independent constraint on $\mathrm{DM_h}$ from Balmer-line measurements (Tendulkar et al. 2017) provide tighter ranges for the host-galaxy and IGM contributions. For FRB 20180916B, the total DM is small enough that a substantially larger $\mathrm{DM_{mw}}$ than provided by the NE2001 model for $\mathrm{DM_{mw,disk}}$ is not allowed, particularly for a larger estimated Galactic halo contribution, $\mathrm{DM_{mw,halo}}$.

To include uncertainties in the disk DM estimate from NE2001, we employ a flat PDF $f_{\mathrm{mw,d}}$(DM) with a 40% spread (i.e., ±20% deviation from the mean) centered on the NE2001 estimate. While larger departures from NE2001 (or YMW16) estimates are seen for some individual Galactic pulsars due to unmodeled H II regions, estimates at Galactic latitudes $|b| \gtrsim 20°$ appear to have much less estimation error, gauged in part by the near agreement of the NE2001 and YMW16 models and also by consistency (in the mean) with parallax distances of high-latitude pulsars (Deller et al. 2019). As a test, using a smaller 20% spread on NE2001 DM values yielded very little change in the final results.

Estimates in the literature for the MW's halo contribution to DM range from 25 pc cm^{-3} to ∼80 pc cm^{-3} (Prochaska & Neeleman 2018; Shull & Danforth 2018; Prochaska & Zheng 2019; Yamasaki & Totani 2020), large enough to impact estimates of extragalactic contributions. Though it has been argued that the MW halo could contribute as little as 10 pc cm^{-3} (Keating & Pen 2020), we conservatively use a flat distribution $f_{\rm mw,h}({\rm DM})$ extending from 25 to 80 pc cm^{-3}. We note however that FRB 20200120E in the direction of M81 (Bhardwaj et al. 2021) shows a total ${\rm DM} = 87.8$ pc cm^{-3} in the direction $(l,\ b) = (142.^{\circ}19,\ 41.^{\circ}2)$. With estimates of ${\rm DM}_{\rm mw,disk} \sim 40$ and 35 pc cm^{-3} for the NE2001 and YMW16 models, respectively, only 48–53 pc cm^{-3} is allowed for ${\rm DM}_{\rm mw,halo} + {\rm DM}_{\rm igm} + {\rm DM}_{\rm M81}$.

Recent work has shown that the burst source is coincident with a globular cluster in the M81 system (Kirsten et al. 2022), so the disk of M81 and the globular cluster make no or little contribution to the DM. If we take the assumed minimum MW halo contribution of ${\rm DM}_{\rm mw,halo} = 25$ pc cm^{-3}, only 23–28 pc cm^{-3} are contributed by M81's halo along with a minimal contribution from the IGM. An alternative reckoning is to attribute ${\rm DM}_{\rm igm} \lesssim 1$ pc cm^{-3} using the mean cosmic density n_{e_0} (next subsection) and the 3.6 Mpc distance to M81, leaving a total of $\lesssim$53 pc cm^{-3} for the summed contributions of the MW and M81 halos. While the halo of M81 may be smaller and less dense than that of the MW, FRB 20200120E provides constraints that are not inconsistent with our adoption of 25 pc cm^{-3} as the minimum of the MW's halo contribution.

In our analysis we marginalize over the total MW DM contribution using the PDF for the sum ${\rm DM}_{\rm mw,disk} + {\rm DM}_{\rm mw,halo}$, which is the convolution of the disk and halo PDFs, $f_{\rm DM,mw}({\rm DM}) = f_{\rm mw,d} * f_{\rm mw,h}$, which is trapezoidal in form.

2.2. Intergalactic Medium Contribution

The FRBs analyzed in this paper have redshifts $z < 1$, so it is reasonable to consider the IGM to be almost completely ionized. We calculate the IGM term using a nominal electron density for the diffuse IGM at $z = 0$ given by a fraction $f_{\rm igm}$ of the baryonic contribution to the closure density, $n_{e_0} = 2.2 \times 10^{-7}$ cm$^{-3} f_{\rm igm}$, evaluated using cosmological parameters from the Planck 2018 analysis implemented in `Astropy`. Shull & Danforth (2018) specify a fiducial range $f_{\rm igm} \approx 0.6 \pm 0.1$ for the baryon fraction although Yamasaki & Totani (2020) adopt a range [0.6, 0.9] consistent with an earlier conclusion that $f_{\rm igm} > 0.5$ (Shull et al. 2012). Measurements of the kinematic Sunyaev–Zel'dovich effect (e.g., Hill et al. 2016; Kusiak et al. 2021) demonstrate consistency of the baryon fraction with Big Bang nucleosynthesis by attributing the apparent deficit of baryons near galaxies to the presence of ionized gas. Those results suggest $f_{\rm igm} \sim 0.8$ according to the baryon budget presented in Shull et al. (2012, Figure 10) in agreement with Zhang (2018). In this paper, we consider a range of values $0.4 \leqslant f_{\rm igm} \leqslant 1$ for most of the analysis but adopt $f_{\rm igm} = 0.85$ when a specific nominal value is needed. We also show that a value of ∼0.85 minimizes the bias and minimum error for a combined dispersion–scattering redshift predictor for the sample of FRBs that have both redshift and scattering measurements.

For a constant comoving density, the IGM makes a mean contribution

$$\begin{aligned}\overline{\rm DM}_{\rm igm}(z) &= n_{e_0} D_{\rm H} \int_0^z dz' \frac{(1+z')}{E(z')} \\ &\equiv n_{e_0} D_{\rm H} \tilde{r}_1(z) \approx 972 \ {\rm pc\ cm^{-3}} f_{\rm igm}\, \tilde{r}_1(z), \end{aligned} \qquad (2)$$

where $D_{\rm H} = c/H_0$ is the Hubble distance and $E(z) = [\Omega_{\rm m}(1+z)^3 + 1 - \Omega_{\rm m}]^{1/2}$ for a flat ΛCDM universe with a matter density $\Omega_{\rm m}$. The second equality defines the integral $\tilde{r}_1(z)$, where $\tilde{r}_1 \simeq z$ for $z \ll 1$.

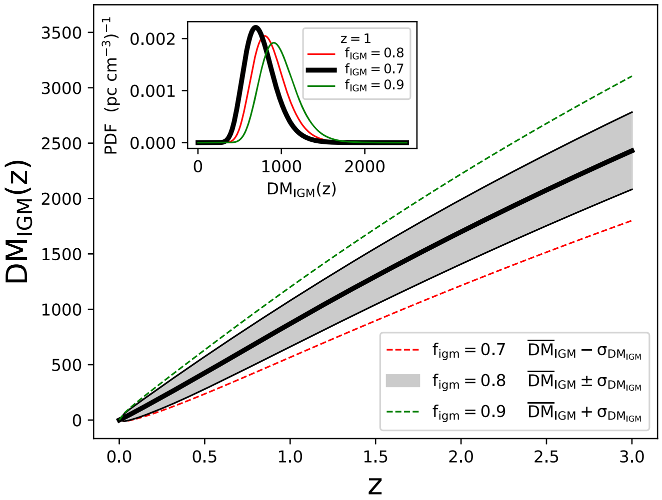

Figure 1. Modeled IGM contribution to DM as a function of redshift for three values of the baryonic fraction, $f_{\rm igm}$. The gray band shows $\overline{\rm DM}_{\rm igm}(z) \pm \sigma_{\rm DM_{igm}}(z)$ for $f_{\rm igm} = 0.8$ while the dashed green line is the upper range $\overline{\rm DM}_{\rm igm}(z) + \sigma_{\rm DM_{igm}}(z)$ for $f_{\rm igm} = 0.9$ and the dashed red line is the lower range $\overline{\rm DM}_{\rm igm}(z) + \sigma_{\rm DM_{igm}}(z)$ for $f_{\rm igm} = 0.7$. The inset shows the PDF of ${\rm DM}_{\rm igm}$ at $z = 1$ for the three values of $f_{\rm igm}$.

The cosmic variance of the IGM density (e.g., McQuinn 2014) produces variations in DM characterized as a zero-mean process $\delta{\rm DM}_{\rm igm}$ with a distance-dependent rms, $\sigma_{\rm DM_{igm}}(z)$. We approximate the results of cosmological simulations by adopting a simple scaling law,

$$\sigma_{\rm DM_{igm}}(z) = [\overline{\rm DM}_{\rm igm}(z) {\rm DM}_{\rm c}]^{1/2}, \qquad (3)$$

where ${\rm DM}_{\rm c} = 50$ pc cm^{-3}. For $z = 1$ this gives $\sigma_{\rm DM_{igm}}(1) = 233 f_{\rm igm}^{1/2}$ pc cm^{-3}. We obtained results by increasing ${\rm DM}_{\rm c}$ to 100 pc cm^{-3}, i.e., a 41% increase in $\sigma_{\rm DM_{igm}}$, and found little change in the net results described in the rest of the paper.

Our scaling law implies a decrease in the fractional variation of $\overline{\rm DM}_{\rm igm}$ with increasing redshift as $\sigma_{\rm DM_{igm}}(z) / \overline{\rm DM}_{\rm igm}(z) = [{\rm DM}_{\rm c} / \overline{\rm DM}_{\rm igm}(z)]^{1/2}$, which is consistent with simulation results reported by Ioka (2003), Inoue (2004), McQuinn (2014), and Dolag et al. (2015), although there is considerable uncertainty related to the number of halos encountered along an LoS and their sizes. This is exemplified in Pol et al. (2019), who report substantially different DM distributions between uniform weighting and matter-weighted LoS integrals. Simulations also indicate a substantial skewness of ${\rm DM}_{\rm igm}$ toward larger values.

The cosmic variance in ${\rm DM}_{\rm igm}$ is implemented using a redshift-dependent PDF $f_{\rm DM,igm}({\rm DM}_{\rm igm}; z,\ f_{\rm igm})$ that is log-normal in form, $\mathcal{N}(\mu,\ \sigma)$ with parameters

$$\sigma = \{\ln[1 + (\sigma_{\rm DM_{igm}} / \overline{\rm DM}_{\rm igm})^2]\}^{1/2}, \qquad (4)$$

$$\mu = \ln \overline{\rm DM}_{\rm igm} - \sigma^2/2. \qquad (5)$$

The skewness of the distribution, $\gamma = (e^{\sigma^2} + 2)\sqrt{e^{\sigma^2} - 1}$, decreases with redshift and so is at least qualitatively consistent with the published simulations cited above.

Figure 1 shows ${\rm DM}_{\rm igm}(z)$ for $f_{\rm igm} = 0.8 \pm 0.1$ using the parameterization of Equations (2) and (3). The inset shows the PDFs of ${\rm DM}_{\rm igm}$ at $z = 1$ for the same values of $f_{\rm igm}$. The cosmic variance in ${\rm DM}_{\rm igm}$ implies considerable variations in DM-derived values of redshift even if the baryonic fraction $f_{\rm igm}$ is known. Likewise, uncertainties in $f_{\rm igm}$ exacerbate those of DM-derived redshifts. In a later section, we demonstrate that scattering measurements can further improve redshift estimates as well as constrain the value of $f_{\rm igm}$.

2.3. Posterior PDF for DM$_h$ for FRBs with Redshifts

A frequent assumption that appears in the FRB literature is a constant host-galaxy contribution to DM, often with a value $\mathrm{DM}_{\rm h}^{(\rm assumed)} = 50\ \mathrm{pc\ cm^{-3}}$ (e.g., Arcus et al. 2021 and references therein) accompanied by a statement that a range of values does not matter in an analysis of mostly large FRB DMs. We find that this is not the case for published FRBs with associated galaxy redshifts. Indeed, our conclusion is underscored by the discovery of the low-redshift FRB 190520 with a large total DM ($z = 0.241$, $\mathrm{DM} = 1202\ \mathrm{pc\ cm^{-3}}$), which requires a large DM$_{\rm h}$ (Niu et al. 2021). In this paper, a necessary step is to calculate the Bayesian posterior PDF for each FRB.

We wish to estimate the DM$_{\rm h}$ contributed by a host galaxy (in its rest frame) taking into account uncertainties in the MW and IGM contributions. We assume that measurements of the DM and redshift z have negligible error. From Equation (1) the conditional PDF for DM$_{\rm h}$ is

$$f_{\mathrm{DM_h}}(\mathrm{DM_h}|\mathrm{DM},\, \mathrm{DM_{mw}},\, z_{\rm h}) = (1 + z_{\rm h})^{-1} f_{\rm DM,igm}(\mathrm{DM} - \mathrm{DM_{mw}} - \mathrm{DM_h}/(1 + z_{\rm h})). \quad (6)$$

Marginalization over the PDF $f_{\rm DM,mw}$ for the MW contribution DM$_{\rm mw}$ then gives $f_{\mathrm{DM_h}}(\mathrm{DM_h}|\mathrm{DM},\, z_{\rm h})$.

Figure 2 shows the PDF $f_{\mathrm{DM_h}}$ and the corresponding cumulative distribution function (CDF) for four selected objects and four different values for the baryonic fraction, $f_{\rm igm}$. The FRBs include FRB 20200120E with a very small total DM compared to another with a potentially large host-galaxy DM, FRB 20190523A. Due to the proximity of FRB 20200120E, different assumed values for the baryonic fraction yield negligible changes in the estimates of DM$_{\rm h}$ because the IGM contributes very little to DM. However, changes in DM$_{\rm igm}$ and thus DM$_{\rm h}$ are of order 100–200 pc cm^{-3} for FRB 20121102A and FRB 20200430A and several hundred pc cm^{-3} for FRB 20190523A for different values of $f_{\rm igm}$. The range of DM$_{\rm h}$ for FRB 20121102A is consistent with that found from the analysis of Balmer lines (Bassa et al. 2017; Tendulkar et al. 2017), designated by the shaded band in the figure.

Table 2 gives the DM inventory for all of the FRBs from Table 1. Columns (1)–(3) give the FRB name, measured DM, and host redshift. The next eight columns give the DM and credible range for the MW, IGM, and host-galaxy contributions. The last three columns give redshift estimates using only the DM inventory, as discussed in Section 5.1. In that section, the DM-based redshifts are compared with those obtained using a combined scattering–DM redshift estimator.

The LoS to FRB 20200120E, the FRB in a globular cluster associated with M81, evidently does not sample the disk of M81. Using the PDF for the MW contribution from the disk and halo and the negligible contribution from the diffuse IGM, the halo of M81 is found to contribute a DM of $\mathrm{DM_{M81,halo}} = 13^{+21}_{-8}\ \mathrm{pc\ cm^{-3}}$.

The posterior PDFs for host-galaxy DMs are combined in Figure 3, which shows the global PDF and CDF for 13 objects (excluding FRB 20200120E) using five values for $f_{\rm igm}$, including a value of 1.2 that exceeds the nominal limit for the diffuse IGM. Note again that DM$_{\rm h}$ is defined in the host-galaxy frame, not the observer's frame. The PDF shifts to larger values of DM$_{\rm h}$ for larger $f_{\rm igm}$. We find the range $f_{\rm igm} \simeq 0.85 \pm 0.05$ to be a good representation of our overall results (see Section 5.2). For $f_{\rm igm} = 0.85$, the 68% credible interval is $\mathrm{DM_h} = 166^{+122}_{-100}\ \mathrm{pc\ cm^{-3}}$, a result that is not inconsistent with those of James et al. (2022). The CDF implies that about 5% of FRBs will show $\mathrm{DM_h} \gtrsim 400\ \mathrm{pc\ cm^{-3}}$. The discovery of FRB 20190520B with an implied DM$_{\rm h}$ well in excess of 400 pc cm^{-3} (Niu et al. 2021) will extend the tail of the global PDF further but is not overly inconsistent with the statistics of the sample we have analyzed in Table 1. A detailed analysis of FRB 20190520B is given in Ocker et al. (2022a).

3. Scattering Inventory

The scattering time τ is the other propagation observable that constrains intervening plasmas. The scintillation bandwidth $\Delta\nu_{\rm d} \simeq (2\pi\tau)^{-1}$ yields the same information, though in practice it has only been measured convincingly for scintillation caused by Galactic scattering (e.g., Masui et al. 2015; Gajjar et al. 2018; Hessels et al. 2019; Bhandari et al. 2020; Marcote et al. 2020) whereas directly measured pulse broadening has been identified primarily from scattering that is extragalactic in origin except for FRB 20180916B, which shows Galactic scattering with $\tau = 46 \pm 10$ ms at 0.15 GHz (Pastor-Marazuela et al. 2021) that is consistent with scintillation bandwidths measured at higher frequencies.

Contributions to scattering times from different media along the LoS are additive (see Equation (A2)). Parallel to the DM inventory in Equation (1), we expand τ into terms involving the MW (disk and halo), the IGM, a possible intervening galaxy or halo, and a host galaxy (including its halo),

$$\tau(\nu) = \tau_{\rm mw}(\nu) + \tau_{\rm igm}(\nu, z) + \frac{\tau_{\rm igh}(\nu)}{(1 + z_{\rm igh})^{x_\tau - 1}} + \frac{\tau(\nu)}{(1 + z_{\rm h})^{x_\tau - 1}}, \quad (7)$$

where we adopt a power-law frequency scaling, $\tau(\nu) \propto \nu^{-x_\tau}$, with an index $x_\tau \simeq 4$. The redshift scalings in the last two terms of Equation (7) take into account that scattering occurs at $\nu' = \nu(1 + z)$ in a galaxy's rest frame for an observation frequency ν and that dilation of the observed scattering time is by a factor $(1 + z)$ (see also Macquart & Koay 2013).

In the following, we develop a model for scattering media and compare it against Galactic pulsar measurements. We argue that only the disk components of galaxies contribute significantly to scattering while galaxy halos and the IGM contribute negligibly.

3.1. The τ–DM Relation for Galactic Scattering

We incorporate much of what has been learned about temporal scattering from Galactic pulsars. Figure 4 shows scattering times plotted against DM for 568 pulsars, including upper limits, using data from the literature. Scattering times from different radio frequencies have been scaled to 1 GHz using a scaling law with $x_\tau = 4$.

Multifrequency observations yield a range of roughly $3 \lesssim x_\tau \lesssim 4.5$ for the power-law index x_τ, whereas idealized models of diffraction from small-scale density fluctuations in the interstellar plasma indicate $x_\tau = 4$ (e.g., Scheuer 1968; Rickett 1990) or $x_\tau = 2\beta/(\beta - 2) = 4.4$ for the simplest form of

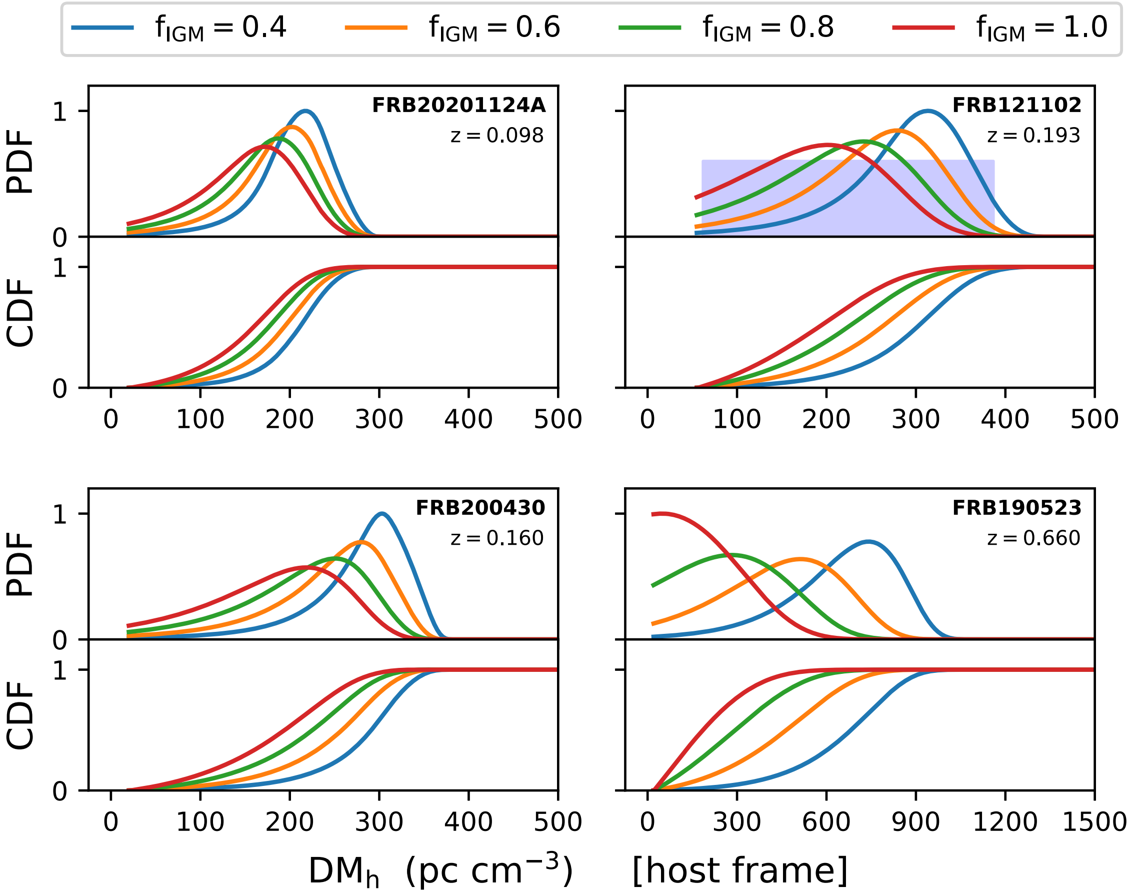

Figure 2. Posterior PDF and CDF for DM$_{\rm h}$ (in the host galaxy's frame) for four selected FRBs and four values of the IGM's baryonic fraction $f_{\rm igm}$. PDFs are normalized to unit maximum. A minimum value, DM$_{\rm h,min}$ = 20 pc cm^{-3}, has been imposed as a prior on DM$_{\rm h}$ except for FRB 20121102A, for which 50 pc cm^{-3} was used. Results are not sensitive to this minimum except for FRB 20200120E (not shown), which has a small extragalactic contribution to DM. The shaded region for FRB 20121102A designates the constraint on DM$_{\rm h}$ from Balmer-line measurements (Bassa et al. 2017; Tendulkar et al. 2017).

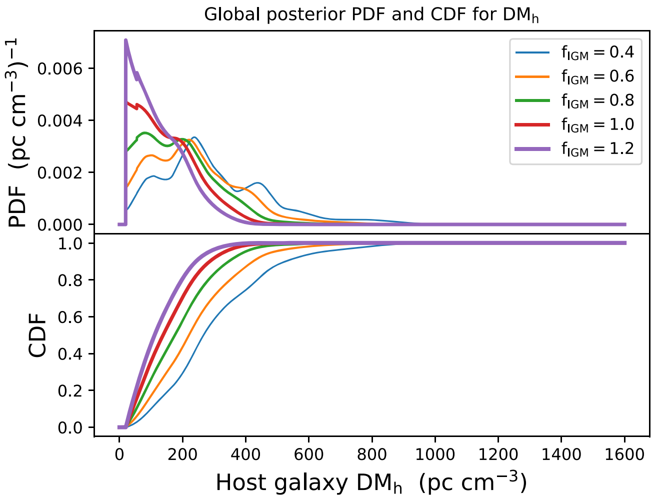

Figure 3. Composite PDF and CDF of host-galaxy DM$_{\rm h}$, calculated for five values of the fraction of baryons $f_{\rm igm}$ in the diffuse IGM. The composite PDF is the unweighted sum of the posterior PDFs for the FRBs in Table 1 with FRB 20200120E excluded due to its special geometry with respect to M81.

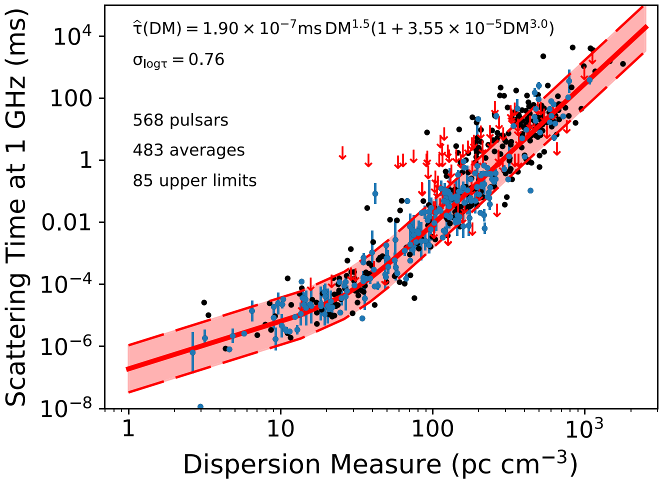

Figure 4. τ vs. DM for Galactic pulsars. The fitted line (solid red) and $\pm 1\sigma$ variations (dashed red) are based on measurements and upper limits on τ for Galactic pulsars. Blue points with error bars are averages over multiple measurements while black points are single measurements from the literature. The plotted pulsar values are from numerous literature sources and are available on request from the corresponding author.

Kolmogorov fluctuations with a wavenumber spectral slope $\beta = 11/3$. Departures from $x_\tau = 4.4$ are expected if the inner scale for the fluctuations is larger than the diffraction scale (Spangler & Gwinn 1990; Bhat et al. 2004; Rickett et al. 2009), or if scattering is anisotropic (e.g., Brisken et al. 2010). Scattering regions that are finite in size transverse to the LoS also alter the scaling law (Cordes & Lazio 2001). These effects invariably reduce x_τ from the simple Kolmogorov value. Keeping this variety of scaling exponents in mind, we

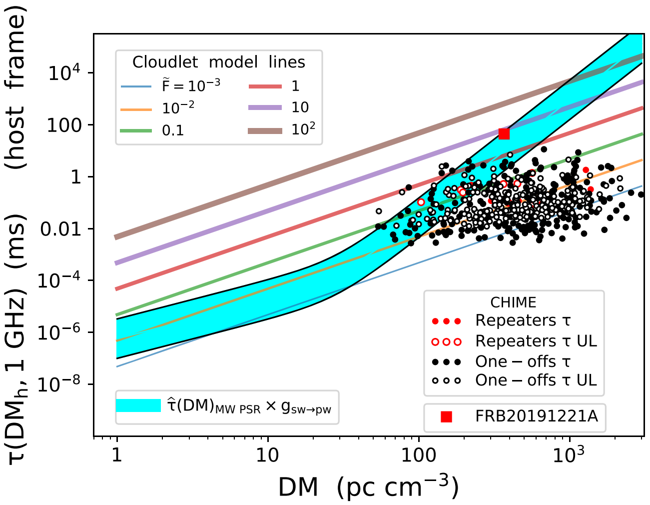

Figure 5. Scattering time τ vs. DM. The cyan band shows the range of scattering times seen from Galactic pulsars evaluated using $\pm\sigma_{\log_1 0(\tau)} = 0.76$ about the mean curve. The τ–DM relation for pulsars from Figure 4 is shown here after shifting it upward to account for plane-wave scattering relevant to FRBs (see text). Lines show the scattering time for the cloudlet model of Equation (A6) for different values of the fluctuation parameter $\widetilde{F}$ (Equation (A4)). The units of $\widetilde{F}$ are (pc^2 km)$^{-1/3}$. Applying the relation to a host galaxy then requires that the DM axis correspond to DM$_\mathrm{h}$, the host galaxy's contribution, and the τ axis is in the rest frame of the host galaxy. Also shown are FRBs from the CHIME FRB catalog (Amiri et al. 2021) (black points) The large red square is for the heavily scattered FRB 20191221A detected with CHIME (The CHIME/FRB Collaboration et al. 2021). For plotting the FRB points, the total DM has been used, which includes Galactic and IGM contributions in addition to the host-galaxy contribution.

adopt $x_\tau = 4$ as a fiducial value. This value is also consistent with the multifrequency analysis of Bhat et al. (2004) and Krishnakumar et al. (2015). Fitting a function $\hat{\tau}(\mathrm{DM}) = A \times \mathrm{DM}^a(1 + B \times \mathrm{DM}^b)$ (Ramachandran et al. 1997) to the pulsar data yields the scattering–DM relation for Galactic pulsars at frequencies ν in GHz,

$$[\hat{\tau}(\mathrm{DM}, \nu)]_{\mathrm{mw,psr}} = 1.90 \times 10^{-7}\ \mathrm{ms} \times \nu^{-x_\tau} \mathrm{DM}^{1.5} \times (1 + 3.55 \times 10^{-5}\ \mathrm{DM}^{3.0}), \tag{8}$$

with scatter $\sigma_{\log\tau} = 0.76$ (Bhat et al. 2004; Cordes & Chatterjee 2019). The fit is shown in Figure 4 as a red band with a centroid line given by Equation (8) and the upper and lower boundaries corresponding to $\pm 1\ \sigma_{\log\tau}$. The band steepens significantly at large DMs, a feature that is due to the larger density fluctuations in the inner Galaxy, where large-DM pulsars are located, compared to those near the solar system or in the outer galaxy (Cordes et al. 1991; Cordes & Lazio 2002).

The measured scattering times necessarily include the fact that Galactic pulsars are embedded in the interstellar scattering medium. The same medium will scatter FRBs but by larger amounts because of their much larger distances. The difference between spherical wavefronts from Galactic pulsars and plane waves from distant extragalactic FRBs amounts to an increase by a factor $g_{\mathrm{sw}\to\mathrm{pw}} = 3$ in the scattering time. The same holds true for FRBs scattered by their host galaxies by reciprocity (or by the time reversal of propagation).

Figure 5 shows the distribution of τ versus DM for Galactic pulsars after applying this geometrical correction. The cyan band in Figure 5 is a schematic depiction of the fit to Galactic pulsars. Also shown are scattering times from FRBs in the first CHIME catalog of 535 distinct FRBs and a measurement of the largest measured scattering for FRB 20191221A (The CHIME/FRB Collaboration et al. 2021), $\tau(0.6\ \mathrm{GHz}) = 340 \pm 10$ ms or τ (1 GHz) $\simeq 44 \pm 1.3$ ms. This latter point is included to show the wide range of values for FRB scattering.

The abscissa in Figure 5 should in principle stand for the DM of the relevant extragalactic scattering medium with any redshift correction due, but of course, we do not know the redshifts of most FRBs. Using the nominal total DM values shows a long-recognized feature (e.g., Cordes & Chatterjee 2019) of FRB scattering that they are "underscattered" compared to Galactic pulsars. This signifies that the scattering properties of a significant portion of the total DMs are deficient in scattering strength.

We further analyze FRB scattering in terms of a parameterized cloudlet model for the scattering medium.

3.2. τ(DM) for an Ionized Cloudlet Medium

As implied by the τ–DM relation for Galactic pulsars, free electrons both disperse and scatter pulses and bursts. However, while all nonrelativistic free electrons cause dispersion, scattering requires small-scale density fluctuations that are likely very different in warm $\sim 10^4$ K plasma and hot-phase gas ($>10^6$ K). Consequently, we expect the τ–DM relation to differ greatly between interstellar media in galaxies and hot, tenuous plasma in galaxy halos and in the IGM. This is demonstrated to be the case using existing scattering measurements.

To model the scattering medium in any one component (e.g., the MW, a host or intervening galaxy, or subregions within galaxies, such as H II complexes), we use a population of small clouds of ionized gas, each with internal density fluctuations. Following the formalism first presented in Cordes et al. (1991) and further developed by Taylor & Cordes (1993), Cordes & Lazio (2002), Cordes et al. (2016), Macquart & Koay (2013), and Ocker et al. (2020, 2021), cloudlets have internal electron densities $\bar{n}_\mathrm{e}$ and fractional rms density fluctuations $\varepsilon = \sigma_{n_\mathrm{e}}/\langle\bar{n}_\mathrm{e}\rangle \leqslant 1$ (angular brackets denote ensemble average). Variations between cloudlets are given by $\zeta = \langle\bar{n}_\mathrm{e}^2\rangle/\langle\bar{n}_\mathrm{e}\rangle^2 \geqslant 1$. Cloudlets have a volume-filling factor f. We assume internal fluctuations follow a power-law spectrum $\propto C_n^2 q^{-\beta} \exp[-(2\pi q/l_\mathrm{i})^2]$ for wavenumbers $2\pi/l_\mathrm{o} \leqslant q \lesssim 2\pi/l_\mathrm{i}$, where l_o and $l_\mathrm{i} \ll l_\mathrm{o}$ are the outer and inner scales, respectively. We use a Kolmogorov spectrum with $\beta = 11/3$ as a reference spectrum.

The resulting broadening time from a layer with dispersion depth DM$_\ell$ is derived in the Appendix,

$$\tau(\mathrm{DM}_\ell, \nu) = C_\tau \nu^{-4} A_\tau \widetilde{F} G\ \mathrm{DM}_\ell^2 \simeq 0.48\ \mathrm{ms} \times \nu^{-4} A_\tau \widetilde{F} G \times \mathrm{DM}_{100}^2, \tag{9}$$

with ν in GHz and $\mathrm{DM}_{100} \equiv \mathrm{DM}_\ell/(100\ \mathrm{pc\ cm^{-3}})$. The quantity C_τ is a numerical constant defined in the Appendix. The quantity A_τ depends on the inner scale l_i and spectral index β and accounts for the shape of the pulse-broadening function, as described in the Appendix. It can range from $\sim 1/6$ to unity. Other parameters that characterize density fluctuations combine into the quantity

$$\widetilde{F} = \frac{\zeta\varepsilon^2}{f(l_\mathrm{o}^2 l_\mathrm{i})^{1/3}}, \tag{10}$$

which has units of (pc^2 km)$^{-1/3}$ for the outer scale in parsecs and the inner scale in kilometers. The location of the scattering

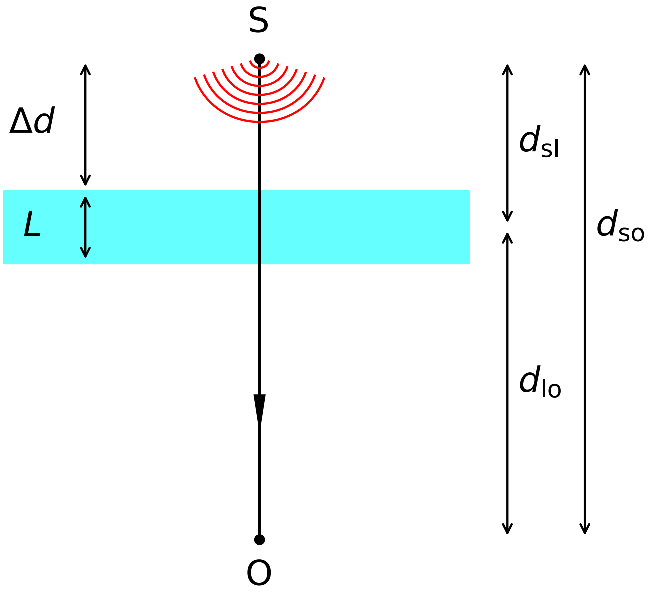

Figure 6. Scattering geometry for a single layer of thickness L and offset from the source by Δd. Its midpoint is a distance $d_{\rm sl}$ from the source and $d_{\rm lo} = d_{\rm so} - d_{\rm sl}$ from the observer. This can represent a source behind its host galaxy, or it could represent an intervening galaxy as in Figure 7.

layer relative to the source strongly affects τ and determines the geometric factor, G (see next section). In most of our analysis, the composite quantity $A_\tau \widetilde{F} G$ is constrained by observations, though we expect $G = 1$ for the LoSs considered in this paper.

For cosmological distances, a source at redshift $z_{\rm s}$ and a scattering region in a host or intervening galaxy at z_ℓ gives

$$\tau(\mathrm{DM}_\ell, \nu, z_\ell, z_{\rm s}) \simeq 0.48\ \mathrm{ms} \times \frac{A_\tau \widetilde{F} G(z_\ell, z_{\rm s}) \mathrm{DM}^2_{l,100}}{\nu^4 (1 + z_\ell)^3}. \tag{11}$$

Here DM_ℓ is in the rest frame of the scattering layer (i.e., a host or intervening galaxy or halo), which contributes to the measured DM as $\mathrm{DM}_\ell/(1 + z_\ell)$.

3.2.1. Scattering Geometries

We define the dimensionless geometric factor G so that it is unity for a source embedded in the scattering medium, such as its host galaxy, and the source distance is much larger than the thickness of the scattering medium. Generally, G is a strong function of the LoS distribution of scattering electrons and can exceed unity by many orders of magnitude. In Euclidean space,

$$G = \frac{\int_{\rm layer} ds\, s(1 - s/d)}{\int_{\rm host} ds\, s(1 - s/d)}. \tag{12}$$

For scattering within the MW or in a distant FRB host galaxy $G = 1$, but it is $\gg 1$ for an intervening galaxy or halo.

First, we derive the geometric factor G with reference to the geometry shown in Figure 6 for a statistically homogeneous (i.e., constant C_n^2) layer of thickness L that is offset from the FRB source by Δd. Letting $x = L/d_{\rm so}$ and $y = \Delta d/d_{\rm so}$ for a source–observer distance $d_{\rm so}$ and defining $g(a, b) = \int_a^b ds\, s(1 - s)$, the geometric factor is defined so that $G = 1$ for a slab representing a host galaxy ($y = 0$) or the MW ($y = 1 - x$),

$$G(x, y) = \frac{g(y, x + y)}{g(0, x)} = \frac{1 - 2x/3 + (2y/x)(1 - y - x)}{(1 - 2x/3)}. \tag{13}$$

Treating intervening galaxies and halos as thin slabs ($x \ll 1$) that are close to neither the source nor observer, we have $G \simeq (2y/x)(1 - y) \gg 1$, illustrating that scattering from an intermediately positioned slab yields much greater pulse broadening, all else being equal. The strong dependence of G on y/x suggests that some of the scatter at a fixed DM in the cyan band shown in Figure 4 derives from different pulsars having different concentrations of scattering regions along their LoS. This "Galactic variance" yields different values of G and thus τ for objects with identical values of DM.

Figure 7 shows four scattering configurations involving the MW, a host galaxy, and an intervening galaxy that are likely to be encountered in FRB observations. Two cases apply to an FRB source that is unaffiliated with or on the near side of a host galaxy, and cases are shown with and without an intervening galaxy. While objects discussed in this paper involve only the first two cases in the figure, we also need to dismiss the possibility that the other two cases do not apply to the current sample, as discussed below.

For nonnegligible redshifts, the expression for G is replaced by one involving angular diameter distances, yielding $G(z_\ell, z_{\rm s}) = 2 d_{\rm sl} d_{\rm lo}/L d_{\rm so}$, where $d_{\rm sl}$ and $d_{\rm lo}$ are distances from the source to the scattering layer and from layer to observer, respectively, and $d_{\rm so}$ is the source distance. Figure 8 shows G versus redshift ratio for several values of the source redshift, $z_{\rm s}$, which we take to be the redshift of a host galaxy (though generally a source need not be associated with a galaxy). For low redshifts, G is symmetric about the midpoint where $z_\ell/z_{\rm s} = 1/2$. However, for large source redshifts, G maximizes at progressively smaller values of $z_\ell/z_{\rm s}$, though at intervening redshifts z_ℓ that are still cosmological. This effect enters into any consideration of scattering of high-redshift FRBs, which we defer to another paper in progress (Ocker et al. 2022b).

For scattering in a host galaxy, $d_{\rm lo}/d_{\rm so} \to 1$ and $d_{\rm sl} \to L/2$, yielding $G \to 1$ as with the Euclidean expression. For Gpc distances ($d_{\rm sl}$, $d_{\rm lo}$, $d_{\rm so}$) and $L = 1$ kpc, $G \sim \mathrm{Gpc/kpc} \sim 4 \times 10^5$. However, unless a galaxy disk is encountered with edge-on geometry, the DM_ℓ may be small. Nonetheless, even with $\mathrm{DM}_\ell = 10\ \mathrm{pc\ cm^{-3}}$, the scattering time for an intervening galaxy would be $\tau \simeq 2$ s if $\widetilde{F}$ is similar to Galactic values. This fact can be used to rule out whether any observed scattering occurs in an intervening galaxy instead of a host galaxy if an FRB can be detected along an LoS that intersects a galaxy disk. More likely, given the large implied scattering for nominal parameters, FRB detections would be strongly suppressed along any such LoS, such as those in the two cases shown on the right in Figure 7.

Our results indicate that FRB LoSs that pierce an intervening galaxy disk are unlikely to be seen at frequencies $\nu \lesssim 1.5$ GHz because the scattering is much larger than the intrinsic burst width. If only a halo is intersected, the FRB's DM will be enhanced but the scattering will not increase significantly.

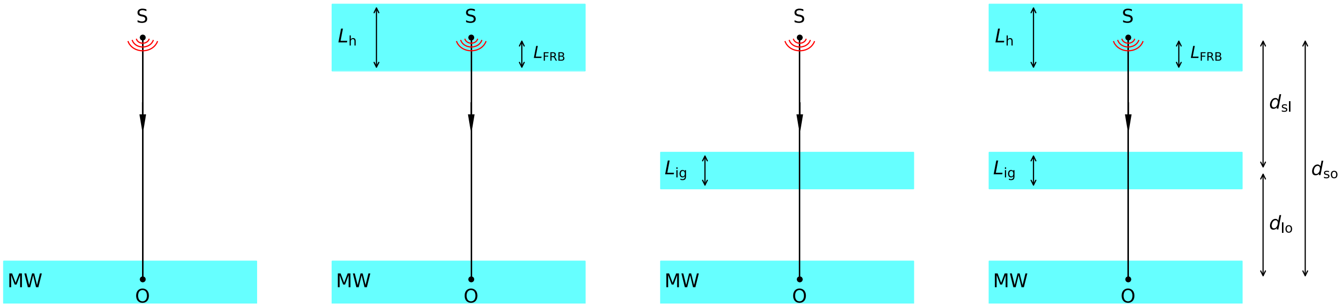

Figure 7. Scattering geometries for extragalactic sources that include the MW and cases without and with scattering layers in a host galaxy (h) or intervening galaxy (ig). The direct LoS is shown from source S to observer O. A scattering layer in an intervening galaxy is at a distance $d_{\rm sl}$ from the source and $d_{\rm lo} = d_{\rm so} - d_{\rm sl}$ from the observer. The thickness of the host galaxy $L_{\rm h}$ is generally larger than the path length through the galaxy to the source, $L_{\rm FRB}$.

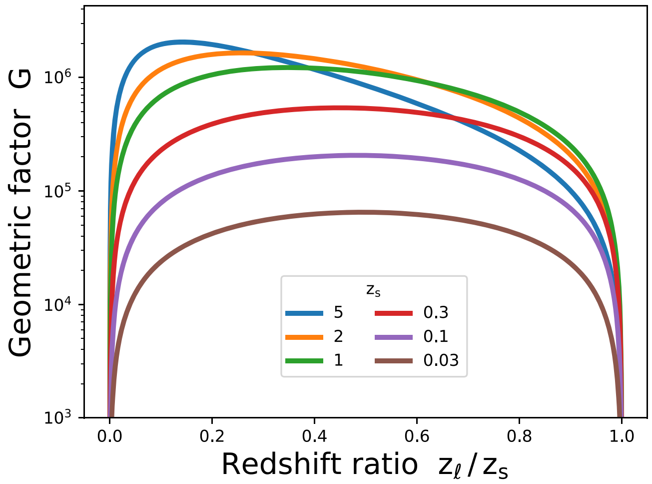

Figure 8. Geometrical factor G vs. redshift ratio for a source at redshift z_s and scattering layer at redshift $z_{\rm l}$. The thickness of the scattering layer is assumed to be $L = 1$ kpc, which is indicative of a galaxy disk. For a thicker layer, $G \propto L^{-1}$ yields a smaller value.

3.2.2. Required Values of $\widetilde{F}G$ for Galactic Pulsars

The quadratic scaling with DM in Equations (9) and (11) (see also Equation (A6)) contrasts with the empirical scaling in Equation (8) for pulsars shown in Figure 5, which has shallower and steeper dependences for small and large DMs, respectively. These differences reflect the strong spatial dependence of $\widetilde{F}$ across the Galaxy because large pulsar DMs necessarily probe the inner part of the Galaxy where Population I activity (e.g., supernovae) is more intense than near the Sun where low-DM pulsars reside (Cordes et al. 1991). The NE2001 model in fact uses values of $l_{\rm i}^{1/3}\widetilde{F}$ that are larger by $\gtrsim$500 in the thin-disk and spiral-arm components compared to the smaller value in the thick disk sampled by low-DM pulsars.

Lines of constant $\widetilde{F}G$ shown in Figure 5 for $\widetilde{F}G = 10^{-3}$ to 10^2 $({\rm pc}^2\ {\rm km})^{-1/3}$ demonstrate that large values are needed to account for the scattering of inner Galaxy pulsars while much smaller values suffice for shorter LoS to pulsars in the solar neighborhood. Pulsars at high Galactic latitudes sample the thick disk of free electrons and yield $\widetilde{F} = (3 \pm 2) \times 10^{-3}$ $({\rm pc}^2\ {\rm km})^{-1/3}$. In addition, Galactic scattering to FRB 20121102A in the anticenter direction places an upper bound $\widetilde{F} \lesssim 3 \times 10^{-2}\,({\rm pc}^2\ {\rm km})^{-1/3}$ for the MW halo, and scattering toward two other FRBs with LoS near or close to galaxy halos yields $\widetilde{F} \lesssim 10^{-3}\,({\rm pc}^2\ {\rm km})^{-1/3}$ for those halos (Ocker et al. 2021).

3.3. Scattering in the IGM

On both observational and theoretical grounds, the IGM's contribution to scattering is likely negligible in comparison with contributions from the interstellar media of galaxy disks, including the MW, host, and intervening galaxies. Not all FRBs with large measured DMs $\gtrsim 10^3\ {\rm pc\ cm}^{-3}$ show large scattering times, which might have been expected if scattering were IGM dominated even with cosmic variance taken into account.

The τ(DM) relation for galaxy disks does not change qualitatively in a cosmological context once redshift dependencies are included, as in Equation (7) (see also Macquart & Koay 2013). Given that the IGM contributes DM values comparable to those of galaxy disks, one might expect scattering to also be similar. However, the $\widetilde{F}G$ factor is likely to be quite different. Assume the product $\zeta\epsilon^2$ is the same because it measures fractional fluctuations that are of order unity in the ISM, and consider equal contributions to the total DM. Ignoring redshift factors, which are close to unity for low-z objects, the ratio of scattering times from the IGM and from a galaxy's ISM is

$$\frac{\tau_{\rm IGM}}{\tau_{\rm ISM}} \approx \frac{[f\,(l_{\rm o}^2 l_{\rm i})^{1/3}]_{\rm ISM}}{[f\,(l_{\rm o}^2 l_{\rm i})^{1/3}]_{\rm IGM}}, \tag{14}$$

where $G = 1$ applies to a source embedded in the ISM of a host galaxy.

The outer scales alone are probably very different because in standard turbulence pictures, they correspond to the scales on which energy is injected. ISM scales are $\lesssim$kpc and IGM scales $\gtrsim$Mpc, giving $\tau_{\rm IGM}/\tau_{\rm ISM} \lesssim ({\rm kpc}/{\rm Mpc})^{2/3} \lesssim 10^{-2}$.

The filling factor and inner scale are also likely larger for the IGM, further reducing the ratio. For example, the inner scale for the solar wind may be linked to the thermal proton gyroradius $r_{g,p} = v_p(T)/\Omega_{g,p}$ (where $v_p(T)$ is the rms thermal speed and $\Omega_{g,p}$ is the gyrofrequency) or to the proton inertial length, $\ell_{i,p} = c/\omega_{p,p}$, where $\omega_{p,p}$ is the proton plasma frequency (Goldstein et al. 2015). These would imply $l_{\rm i} \propto T^{1/2}/B$ or $l_{\rm i} \propto n_{\rm e}^{-1/2}$, respectively. Given the higher temperature, smaller magnetic field, and smaller plasma density of the IGM compared to an ISM, the ratio $\tau_{\rm IGM}/\tau_{\rm ISM}$ might be reduced by another order of magnitude.

Luan & Goldreich (2014) argue similarly that the outer scale for the IGM must be comparable to Galactic values to allow a significant contribution to τ, but they also point out that the resultant turbulent heating would cause the IGM to be hotter than inferred from observations. In the following we therefore exclude any contribution from the diffuse IGM to scattering.

3.4. Scattering in Galaxy Halos

Galactic pulsars show a strong Galactic latitude dependence for scattering times indicative of contributions from a strongly scattering thin disk (Cordes & Lazio 2002; Yao et al. 2017) and a thick disk with a scattering scale height of one-half the scale height $H_{n_e} \sim 1.6$ kpc for the electron density (Ocker et al. 2020). Comparison with the scattering of AGNs, which sample the entire MW halo (unlike pulsars in or near the thick disk or pulsars in the Magellanic clouds), shows no increase in scattering over that provided by the disk components. This implies a modest DM contribution from the Galactic halo along with a small value of $\widetilde{F}G$. We therefore exclude contributions to scattering from the Galactic halo. This may be true for the halos of other galaxies. A specific case is FRB 20200120E in a globular cluster near M81 that likely samples only the halos of M81 and the MW along with the MW disk components. Burst amplitude substructure is seen down to tens of microseconds (combined with shot pulses at the resolution limit of 31.25 ns) that shows no hint of scattering from outside the MW disk (Nimmo et al. 2022).

Nonetheless, given the dynamic processes involved with halo evolution (e.g., Smercina et al. 2020) that might also drive turbulence and the prospects for there being substructure in halos that might also cause radio scattering (Vedantham & Phinney 2019), the possibility is still open that some halos may contribute to scattering.

3.5. Pulse Broadening from the Milky Way

All FRBs have been found from directions where pulse broadening from the MW is too small to detect at observation frequencies larger than 1 GHz but it has been measured at 0.15 GHz for FRB 190816 (Pastor-Marazuela et al. 2021). MW scattering has also been measured in the form of intensity variations with a characteristic scintillation bandwidth $\Delta\nu_{\rm d}$ for several objects (e.g., Masui et al. 2015; Hessels et al. 2019; Bhandari et al. 2020; Marcote et al. 2020). For the low-latitude FRB 20121102A ($b = -0\overset{\circ}{.}2$), the implied scattering is only about $\tau \sim 1/2\pi\Delta\nu_{\rm d} \simeq 20\ \mu$s at 1 GHz for its Galactic anticenter direction, in agreement with the NE2001 prediction within a factor of 2 (Ocker et al. 2021). Future observations will likely probe a wide range of scattering strengths as more bursts are found at low frequencies and low Galactic latitudes.

For the remainder of the paper, we ignore contributions to τ from the MW disk along with those from the halo and from the IGM. As with the DM, we also ignore for now any scattering from intervening galaxies and their halos and also from any intercluster medium, leaving only host galaxies as the main contributor to pulse broadening. The observed scattering time $\tau_{\rm obs}$ is then given by Equation (11) using $\mathrm{DM_h}$ and $z_{\rm g} = z_{\rm s} = z_{\rm h}$. Future studies are likely to include FRBs with significant scattering from the MW. For these cases, the pulse broadening is simply the sum of the contributions from the host galaxy and the MW.

4. Dispersion and Scattering in Host Galaxies

In this section, we present several analyses that provide the basis for redshift estimation using both dispersion and scattering. In the first, we show how the coupling of these two processes in host galaxies depends on redshift if redshift is treated as an independent variable. In the second, we demonstrate that the extragalactic contribution to scattering is most economically understood as originating in host galaxies rather than in intervening galaxies. If that were not the case, values for $A_\tau\widetilde{F}G$ would have to be significantly different from those encountered in the MW and in host galaxies. The third analysis presents joint constraints on the host-galaxy contribution to DM and the scattering parameter, $A_\tau\widetilde{F}G$, to demonstrate their covariance using examples for two FRB values.

4.1. Dispersion and Scattering versus Redshift

The interplay between dispersion, scattering, and redshift is shown in Figure 9 for two cases, FRB 20121102A and FRB 20190523A. In the top panel of each frame, $\mathrm{DM_h}$ is plotted against redshift using Equations (1) and (2) and taking into account cosmic variance in $\mathrm{DM_{igm}}$ as described in Section 2.2. If the redshift were unknown and only the measured DM is available (along with a model for the MW's contribution), a wide range of redshifts is allowed, roughly a factor of 2 in both cases. The actual redshifts shown as vertical red lines indicate a somewhat narrow range for $\mathrm{DM_h}$ for FRB 20121102A but a much wider range for FRB 20190523A.

The bottom panels show how the scattering time estimate depends on redshift (using Equations (7) and (9)), again taking into account cosmic variance in $\mathrm{DM_{igm}}$, but including a wide range for $A_\tau\widetilde{F}G$ in the host galaxy. This "interstellar variance" expands the range of possible scattering times. The upper bound on τ for FRB 20121102A is compatible with this range while the measured τ for FRB 20190523A is at the high end of the range of $A_\tau\widetilde{F}G$ at the measured redshift but overall is not inconsistent with the predicted ranges when the cosmic variance of $\mathrm{DM_{igm}}$ is also taken into account.

4.2. Scattering in Host versus Intervening Galaxies

Next we compare scattering in host galaxies with that in intervening galaxies. As shown in Figure 8, the geometric factor used in Equation (11) that enhances scattering is orders of magnitude larger for an intervening galaxy compared to $G = 1$ in a host galaxy. A consequence is that $\widetilde{F}$ needs to be proportionately smaller in intervening galaxies if they are not to cause scattering times vastly exceeding measured values. These very small values of $\widetilde{F}$ would imply that intervening galaxies can produce significant contributions to DM without corresponding scattering times like those derived from pulsars in the MW. This in turn would require an explanation for why FRBs sample dispersive gas in intervening galaxies with significantly different turbulence properties. A simpler hypothesis is that extragalactic scattering occurs in host galaxies, not in any intervening galaxies in the sample we have analyzed.

To compare host and intervening galaxies, we define a scaled scattering time,

$$\widetilde{\tau} = \frac{\nu^4}{[\mathrm{DM}_{100}^{\rm obs}]^2}\left(\frac{\tau}{0.48\ \mathrm{ms}}\right) = \frac{A_\tau \widetilde{F} G(z_\ell, z_{\rm s})}{1 + z_\ell}, \tag{15}$$

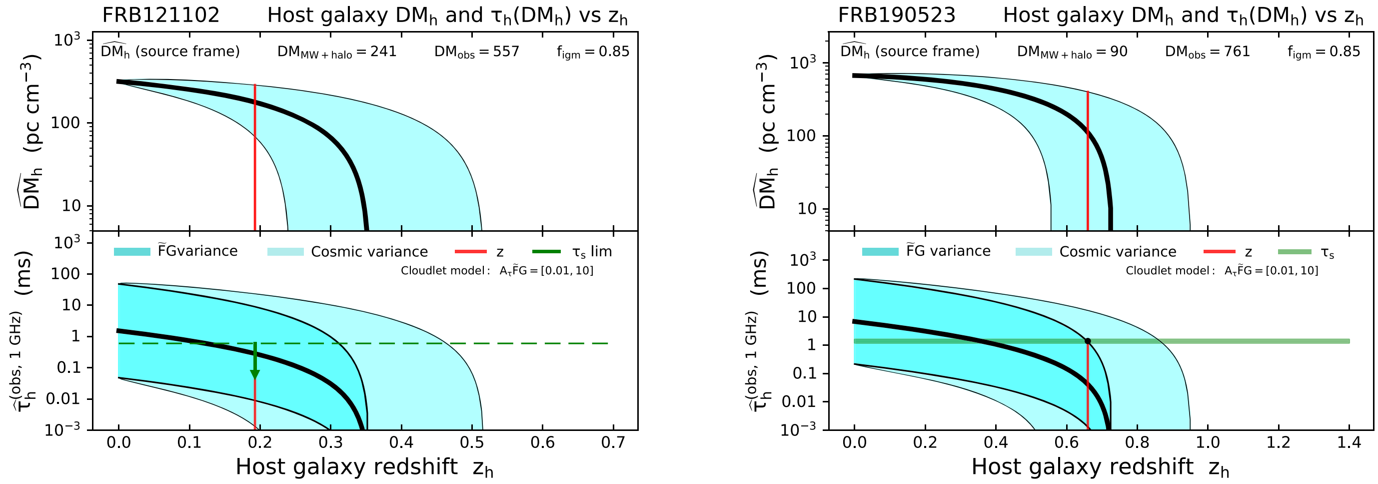

Figure 9. Analysis for FRB 20121102A and FRB 20190523A using the cloudlet model and a baryonic fraction $f_{\rm igm} = 0.85$. Two panels are shown for each FRB: (Top) Host-galaxy DM vs. redshift using the methodology discussed in the text. $\widehat{\rm DM}_{\rm h}$ is expressed in the rest frame of the galaxy and includes uncertainties in the IGM's contribution to the total DM shown as the light-shaded band (cyan). The vertical red line marking the measured redshift shows the range of possible $\rm DM_h$ values; for FRB 20121102A, these are consistent with the results of Tendulkar et al. (2017). (Bottom) Estimated scattering time in the observer's frame at 1 GHz using the cloudlet model discussed in the text. The heavier shaded band indicates the extent of scattering times τ for cloudlet models with $\widetilde{F}G$ in the range [0.1, 10] $(\rm pc^2\ km)^{-1/3}$. The lighter shading indicates the effect on τ of the cosmic variance of the IGM's contribution to $\widehat{\rm DM}_{\rm h}$ shown in the top panel. The green line marks the upper limit (dashed for FRB 20121102A) or measured (solid for FRB 20190523A) scattering time.

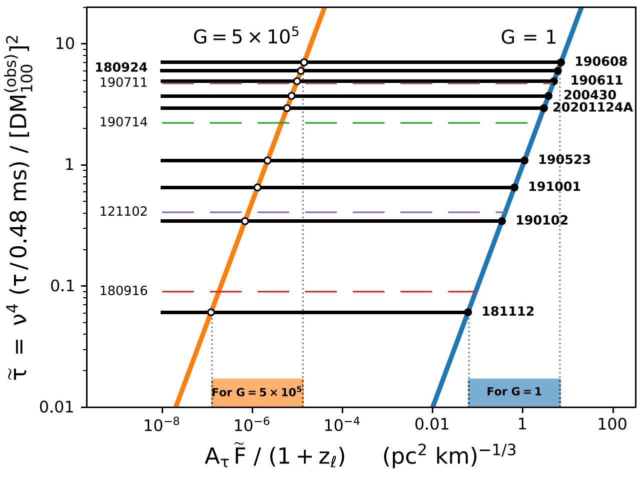

Figure 10. Scaled scattering time $\widetilde{\tau}$ vs. $A_\tau \widetilde{F}/(1+z_\ell)$ (see Equation (15)) where the quantity $\rm DM_{100}^{obs}$ is the observer-frame DM contributed by a "layer" in either a host galaxy or an intervening galaxy (see text). Horizontal lines denote measured values (solid) or upper limits (dashed). The slanted lines show $\widetilde{\tau} \propto G$ for $G = 1$, which applies to scattering in host galaxies, and $G = 5 \times 10^5$, which is a typical value for a 1 kpc thick scattering region in an intervening galaxy midway to the source and at ∼1 Gpc. The horizontal bars at the bottom of the figure indicate the range of values for the abscissa spanned by FRB measurements for each of the two values of G. We exclude the upper limit $\widetilde{\tau} \leqslant 0.0015$ for FRB 20200120E because its LoS is qualitatively different from those of the other FRBs, which are evidently influenced by propagation through their host galaxies.

which involves observable quantities after the first equality and unknown quantities after the second. The redshift of the scattering layer z_ℓ is either that of an intervening galaxy or a region in a host galaxy (with z_ℓ very slightly smaller than $z_{\rm h}$ so that $d_{\rm sl} = L/2$). The DM contributed by the layer $\rm DM_{100}^{obs}$ is expressed in the observer's frame in units of $100\,\rm pc\,cm^{-3}$. Figure 10 shows $\widetilde{\tau}$ versus $A_\tau \widetilde{F} G(z_\ell, z_s)/(1+z_\ell)$ for two values of the geometric factor, $G = 1$, for host galaxies, and $G = 5 \times 10^5$, which is typical for an intervening galaxy at a redshift that maximizes G (see Figure 8). In both cases we have used the inferred $\rm DM_h$ as the DM contributed by the layer expressed in the observer's frame. Measurements and upper limits on $\widetilde{\tau}$ yield a range for the abscissa of $A_\tau \widetilde{F}/(1+z_{\rm h}) \sim 0.018$ to $7.9\ (\rm pc^2\ km)^{-1/3}$ if scattering occurs in host galaxies with $G = 1$ (blue band along the horizontal axis). However, if scattering were to occur in intervening galaxies, the values would be smaller by a factor $(5 \times 10^5)^{-1}$ or $A_\tau \widetilde{F}/(1+z_{\rm h}) \sim 3.6 \times 10^{-8}$ to $1.6 \times 10^{-5}\ (\rm pc^2\ km)^{-1/3}$ (orange band along the horizontal axis). These values are significantly smaller than those that apply to the ISM of the MW, which range from about 10^{-3} to $10\,(\rm pc^2\ km)^{-1/3}$. We conclude that scattering of FRBs with known redshifts occurs in host galaxies with interstellar media similar to those in the MW as gauged by $\widetilde{F}$. Based on this, in Section 5 we adopt a flat prior for $A_\tau \widetilde{F}$ over the range 0.01 to $10\,(\rm pc^2\ km)^{-1/3}$. This is consistent with values in Figure 2 of Ocker et al. (2021) based on measurements of Galactic pulsars.[2]

4.3. Posterior PDFs for $\rm DM_h$ and $\widetilde{F}G$

The PDF of τ given the redshift and host-galaxy $\rm DM_h$ is $\delta(\tau - \widehat{\tau})$ with $\widehat{\tau} = C_\tau \nu^{-4} A_\tau \widetilde{F} G\, {\rm DM}_{\rm h}^2/(1+z)^3$. If the redshift is known to high precision but the measured broadening has an error distribution $f_{\delta\tau}(\tau - \tau_{\rm obs}, \sigma_\tau)$, where $\tau_{\rm obs}$ is a nominal value and σ_τ is the uncertainty, we calculate the likelihood function for $x \equiv \rm DMP_h$ and $\phi \equiv A_\tau \widetilde{F} G$, the two parameters we use to characterize the interstellar medium of a host galaxy,

$$\begin{aligned}\mathscr{L}(x, \phi \mid {\rm DM}, z_{\rm h}, \tau) \\ = f_\tau(\widehat{\tau} \mid {\rm DM_h}, z_{\rm h}) = f_{\delta\tau}(\widehat{\tau} - \tau_{\rm obs}).\end{aligned} \tag{16}$$

---

[2] While Figure 2 of Ocker et al. (2021) shows values of $\widetilde{F}$ extending outside the range we adopt, the bulk of the measurements are in that range. Note also that the values in that paper assume $A_\tau = 1$, so they can alternatively be interpreted as the range for $A_\tau \widetilde{F}$.

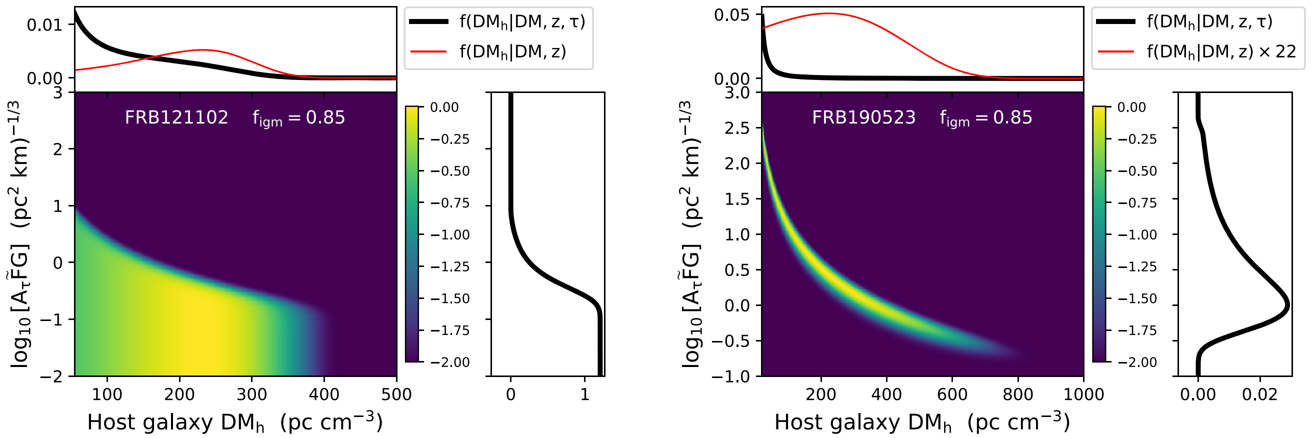

Figure 11. Posterior PDFs for DM$_h$ and $\widetilde{F}G$ for two FRBs. The large panel shows probability density vs. $A_\tau\widetilde{F}G$ and DM$_h$ assuming flat priors for each quantity, with DM$_h$ constrained within 50–500 pc cm^{-3} or 50–1000 pc cm^{-3} for FRB 20121102A and FRB 20190523A, respectively. The ranges for $\log_{10}A_\tau\widetilde{F}G$ are −2 to 3 for FRB 20121102A and −1 to 3 for FRB 20190523A. The black curves in the top and side panels are marginalized, one-dimensional PDFs. The red curves in the top panels are the posterior PDFs for DM$_h$ derived from the DM-inventory analysis of Section 2.3.

Combined with the MW-marginalized PDF for DM$_h$ in Equation (6) and assuming an uninformative flat prior for ϕ, the posterior PDF is

$$f_{\mathrm{DM_h},\phi}(x, \phi|\mathrm{DM}, z_\mathrm{h}, \tau)$$
$$\propto f_{\mathrm{DM_h}}(x|\mathrm{DM}, z_\mathrm{h}) f_\tau(\tau - A_\tau C_\tau \nu^{-4}\phi\, x^2/(1+z)^3). \tag{17}$$

Figure 11 gives two examples of the joint posterior PDFs for x and ϕ using $f_{\mathrm{igm}} = 0.85$ for FRB 20121102A, an object with only an upper limit on scattering, and FRB 20190523A, which has a significant measurement of the scattering time. The flat prior for DM$_h$ extends from 50 pc cm^{-3} in both cases up to different maximum values, 500 pc cm^{-3} and 1000 pc cm^{-3}, respectively.

For FRB 20121102A, the marginalized PDF for $A_\tau\widetilde{F}G$ in the side panel includes a tail to values of $A_\tau\widetilde{F}G$ larger than unity that are still consistent with the upper limit on τ because the corresponding values of DM$_h$ are very small. These small values are strongly disfavored by Balmer-line measurements that indicate DM$_h \sim 55$ to 380 pc cm^{-3} (as indicated in Figure 2). The marginalized PDF for DM$_h$ in the upper panel (black curve) indicates these values along with a wider range extending to ∼400 pc cm^{-3}. The same frame shows in red the posterior PDF for DM$_h$ resulting from the DM inventory also shown in Figure 2.

FRB 20190523A, by comparison, shows a joint PDF with a shape determined by the relationship $\phi = A_\tau\widetilde{F}G \propto \tau\mathrm{DM}_\mathrm{h}^{-2}$. Without other constraints, the LoS through the host galaxy can encounter ionized gas with values for DM$_h$ and $A_\tau\widetilde{F}G$ anywhere along the curved ridge of high probability density. Formally, the broad prior in DM$_h$ allows a solution with small DM$_h$ and a corresponding value for $A_\tau\widetilde{F}G$ much larger (by one or two orders of magnitude) than is encountered in the MW. While it is conceivable there could be such regions along the LoS to an FRB, their required properties run counter to those in the ISM of the MW and other galaxies.

A simpler conclusion is that the actual range of values for DM$_h$ and thus also for $A_\tau\widetilde{F}G$ are significantly smaller than the plotted ranges in Figure 11. In particular, the blue horizontal band in Figure 10 corresponds to values for $A_\tau\widetilde{F}G$ in the interval [0.02, 6] (pc^2 km)$^{-1/3}$, and in the next section, we will use a slightly larger range, [0.01, 10] (pc^2 km)$^{-1/3}$ as one of the flat priors used in redshift estimation.

5. Redshift Estimators

Only a small fraction of the current sample of FRBs has been reliably localized to host galaxies with redshifts, and while efforts are underway to provide routine high-precision localizations of a large number of FRBs with, e.g., CHIME outriggers (Leung et al. 2021; Cassanelli et al. 2022), DSA-2000 (Hallinan et al. 2019), and other facilities, it will take some time for such efforts to come to fruition.

Meanwhile, we assess a method that uses scattering times τ along with DMs to constrain FRB redshifts. The gist of the method is that a host galaxy requires a large-enough DM$_h$ to provide the scattering time given a plausible value for $A_\tau\widetilde{F}G$. The resulting constraints on DM$_h$ in turn yield a plausible range for DM$_{\mathrm{igm}}$ and thus redshift z_h. For the current sample of objects, this approach also provides a test for the actuality of FRB–galaxy associations. In particular, if a candidate host galaxy is at a redshift that implies a small DM$_h$ (because the IGM dominates the DM budget) but the FRB has a large amount of scattering, there are two possibilities. There may be an intervening galaxy that scatters the FRB with a relatively small contribution to DM owing to the geometrical effects discussed in Section 3.2.1. Alternatively, the association may be incorrect with the "intervening" galaxy in the first instance being the actual host galaxy.

5.1. DM-based Redshifts

DM-based redshift estimation follows from previous work (e.g., Macquart et al. 2020) and expressions in Section 2.2. First, we express the DM-based redshift $\hat{z}_{\mathrm{DM}}$ in terms of an assumed value for DM$_h$, either an a priori value or one based on Balmer-line measurements of a host galaxy to determine an emission measure EM from which a galaxy-wide estimate for DM$_h$ is estimated. This implies a point estimate for the IGM's contribution (see Equation (1)),

$$\widehat{\mathrm{DM}}_{\mathrm{igm}} = \mathrm{DM} - \widehat{\mathrm{DM}}_{\mathrm{mw}} - \widehat{\mathrm{DM}}_\mathrm{h}/(1+z), \tag{18}$$

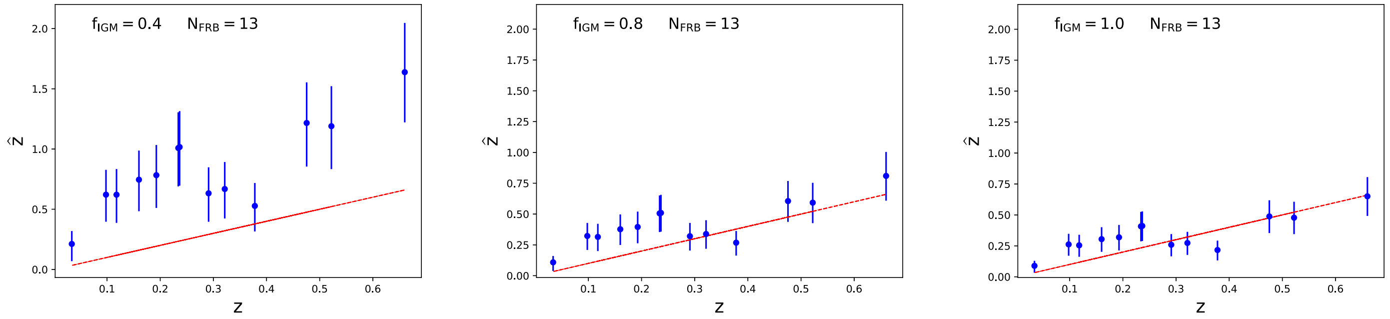

Figure 12. Redshift estimates using only the DM inventory vs. true redshift for 13 FRBs where redshifts are available. The three frames are for $f_{\rm igm} = 0.4$, 0.8, and 1.0 from left to right. Vertical bars represent the 68% credible regions for $\hat{z}$ from the posterior PDFs. The red lines indicate $\hat{z} = z$. FRB 20200120E has been excluded.

that yields a redshift by inverting the function $\tilde{r}_1(z)$ defined in Equation (2),

$$\hat{z}_{\rm DM} = \tilde{r}_1^{-1}(\widehat{\rm DM}_{\rm igm}/n_{e_0}D_{\rm H}) \simeq \widehat{\rm DM}_{\rm igm}/n_{e_0}D_{\rm H}, \qquad (19)$$

where the approximate equality is for small redshifts.

More useful is the posterior PDF for redshift based on a likelihood function,

$$\mathscr{L}(\mathrm{DM_h},\, z|\mathrm{DM};\, f_{\rm igm}) \qquad (20)$$

$$= \delta(\mathrm{DM} - \mathrm{DM_{mw}} - \mathrm{DM_{igm}}(z) - \mathrm{DM_h}(1+z)). \qquad (21)$$

Using a flat, unconstraining prior $f_{z_{\rm h}}(z_{\rm h})$ for the host galaxy's redshift and integrating over prior PDFs for $u = \mathrm{DM_{mw}}$, $v = \mathrm{DM_h}$, and $w = \mathrm{DM_{igm}}$ yields a posterior redshift PDF

$$\begin{aligned} & f_z(z_{\rm h}|\mathrm{DM};\, f_{\rm igm}) \\ & \propto f_{z_{\rm h}}(z_{\rm h}) \iiint du\, dv\, dw\, f_{\rm DM,mw}(u) f_{\rm DM_h}(v) \\ & \quad \times f_{\rm DM,igm}(w,\, z_{\rm h};\, f_{\rm igm})\, \delta(\mathrm{DM} - v/(1+z_{\rm h}) - u - w) \\ & \propto f_{z_{\rm h}}(z_{\rm h}) \iint dv\, dw\, f_{\rm DM_h}(v) f_{\rm DM,igm}(w,\, z_{\rm h};\, f_{\rm igm}) \\ & \quad \times f_{\rm DM,mw}(\mathrm{DM} - v/(1+z_{\rm h}) - w). \end{aligned} \qquad (22)$$

In the following we hold $\mathrm{DM_h}$ fixed at a nominal value to compare our results with the common practice of setting $\mathrm{DM_h} = 50\ \mathrm{pc\ cm^{-3}}$. Other fixed values can also be used, and there is some tradeoff between $f_{\rm igm}$ and a choice for $\mathrm{DM_h}$. However, foreshadowing later results, it is unrealistic to assume a constant value for $\mathrm{DM_h}$ given the wide variety of galaxies found to harbor FRB sources, as well as their different locations in those galaxies and the orientations of those galaxies relative to the LoS.

Figure 12 shows the DM-based redshift estimator plotted against true redshift for 13 objects. This sample excludes FRB 20201120E because its association with M81 makes it too close to the MW to be characterized with a redshift, which is negative. The three panels for baryonic fractions $f_{\rm igm} = 0.4$, 0.8, and 1 demonstrate the much larger bias and scatter for $f_{\rm igm} = 0.4$ (left panel) compared to the two larger values used for the center and right panels. The larger bias and scatter for $f_{\rm igm} = 0.4$ arises because a larger redshift is needed to provide the IGM contribution to DM, on average, when $f_{\rm igm}$ is smaller and the cosmic variance of $\mathrm{DM_{igm}}$ is correspondingly larger. This may be seen from Equation (2), which gives $\overline{\mathrm{DM}}_{\rm igm} \propto f_{\rm igm}\, \tilde{r}_1(z) \propto f_{\rm igm}\, z$ (for $z \ll 1$), which implies that $\hat{z} \propto f_{\rm igm}^{-1}$ × (required $\mathrm{DM_{igm}}$). The rms $\sigma_{\mathrm{DM_{igm}}} \propto \sqrt{f_{\rm igm}\, z}$ translates into an error on $\hat{z}$ that then scales as $\sigma_{\hat{z}} \propto \sqrt{\hat{z}/f_{\rm igm}}$, which is also larger for smaller $f_{\rm igm}$.

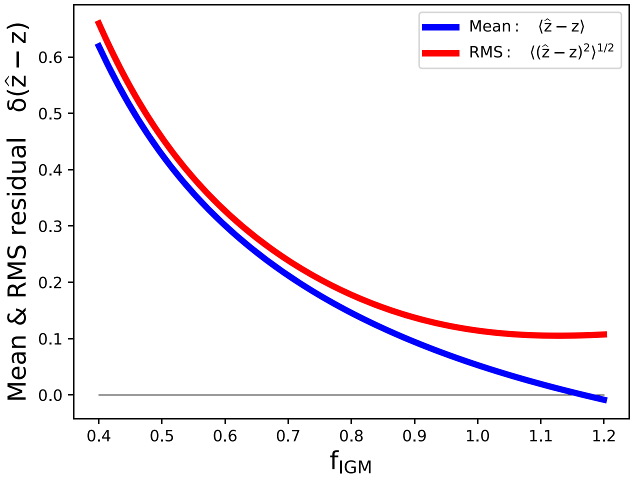

Figure 13. Mean and rms redshift residual vs. baryonic fraction $f_{\rm igm}$ for the DM-only redshift estimator.

As measures of the goodness of fit, we show in Figure 13 the mean residual $\delta z = \langle \hat{z} - z \rangle$, which measures the estimation bias, and the rms residual $\sigma_{\delta\hat{z}} = \langle (\delta z)^2 \rangle^{1/2}$ versus $f_{\rm igm}$. We have used values for $f_{\rm igm}$ that exceed unity here (and in further analyses below) to include the possibility that FRBs reside in regions of atypically high baryon fraction (e.g., Pol et al. 2019). Angular brackets denote a weighted average using weights equal to the reciprocal of the variance of $\hat{z}$ for each FRB (determined from the 68% probability region centered on the median of the posterior CDF). The figure shows these to be monotonically decreasing with larger $f_{\rm igm}$. If a larger fixed value of $\mathrm{DM_h}$ were used instead of $50\ \mathrm{pc\ cm^{-3}}$, the bias would be reduced for the FRBs with $z \lesssim 0.25$ but would increase for larger redshifts.

5.2. DM- and τ-based Redshifts

Scattering can further constrain redshifts if it is measurable and sufficiently large to require a substantial host-galaxy $\mathrm{DM_h}$. For a scattering time τ attributed to a host galaxy at redshift $z_{\rm h}$, the host-galaxy contribution to the DM (in the host frame) is

$$\widehat{\mathrm{DM}}_{\mathrm{h}}(\tau) = \left[\frac{(1+z_{\mathrm{h}})^3\nu^4\tau(\nu)}{C_\tau A_\tau \widetilde{F} G}\right]^{1/2} \simeq 144\ \mathrm{pc\ cm^{-3}}\left[\frac{(1+z_{\mathrm{h}})^3\nu^4\tau_{\mathrm{ms}}(\nu)}{A_\tau \widetilde{F} G}\right]^{1/2}, \qquad (23)$$

for ν in GHz, τ in ms, and $\widetilde{F}$ in $(\mathrm{pc}^2\ \mathrm{km})^{-1/3}$ in the approximate equality. This in turn yields a scattering-based point estimate for $\mathrm{DM}_{\mathrm{igm}}$,

$$\widehat{\mathrm{DM}}_{\mathrm{igm}}(\tau, z_{\mathrm{h}}) = \mathrm{DM} - \widehat{\mathrm{DM}}_{\mathrm{mw}} - \widehat{\mathrm{DM}}_{\mathrm{h}}(\tau)/(1+z_{\mathrm{h}}), \qquad (24)$$

from which a DM–τ-based redshift is estimated by inverting the dimensionless quantity $\tilde{r}_1(z)$ (defined in Equation (2)),

$$\hat{z}_{\mathrm{DM},\tau} = \tilde{r}_1^{-1}(\widehat{\mathrm{DM}}_{\mathrm{igm}}(\tau, z_{\mathrm{h}})/n_{e_0}D_{\mathrm{H}}). \qquad (25)$$

To obtain the posterior redshift PDF we use the likelihood function

$$\mathscr{L}(x, \phi, z|\mathrm{DM}, \tau) = f_\tau(\tau|\mathrm{DM}_{\mathrm{h}}, z) = f_{\delta\tau}(\hat{\tau} - \tau), \qquad (26)$$

where, as before, $f_{\delta\tau}(\delta\tau)$ is the measurement error PDF for the scattering time, $x \equiv \mathrm{DM}_{\mathrm{h}}$, and $\phi \equiv A_\tau \widetilde{F} G$. We marginalize over the joint PDF of x and ϕ and use a prior $f_{z_{\mathrm{h}}}(z_{\mathrm{h}})$ for the host galaxy's redshift,

$$f_z(z_{\mathrm{h}}|\mathrm{DM}, \tau) \propto f_{z_{\mathrm{h}}}(z_{\mathrm{h}}) \iint dx\, d\phi\, f_{\mathrm{DM_h}, A_\tau \widetilde{F} G}(x, \phi) \times f_{\delta\tau}(\tau - A_\tau C_\tau \nu^{-4}\phi\, x^2/(1+z)^3). \qquad (27)$$

Errors in the estimates $\hat{z}_{\mathrm{DM}}$ and $\hat{z}_{\mathrm{DM},\tau}$ are due to the usual uncertainties in the MW contribution to DM, the measurement error in τ, and the astrophysical variance in $\widetilde{F}$ but mostly from cosmic variance in $\mathrm{DM}_{\mathrm{igm}}$ and uncertainty in f_{igm}.

We evaluate Equation (27) using a flat, uninformative redshift prior $f_{z_{\mathrm{h}}}(z_{\mathrm{h}})$ and a flat PDF for $x \equiv \mathrm{DM}_{\mathrm{h}}$ over a range $\mathrm{DM}_{\mathrm{h}} = [20, 1600]\ \mathrm{pc\ cm^{-3}}$. For $\phi \equiv A_\tau \widetilde{F} G$, we use a flat PDF that is sampled at logarithmic intervals over two ranges to provide two different priors for ϕ: a broad range $[\phi_{\mathrm{min}}, \phi_{\mathrm{max}}] = [0.01, 10]\ (\mathrm{pc}^2\ \mathrm{km})^{-1/3}$ and a narrow range, $[0.5, 2]\ (\mathrm{pc}^2\ \mathrm{km})^{-1/3}$. We take this approach to illustrate the effects of alternative priors for the current limited sample of nine objects with scattering measurements and redshifts. The broad range is consistent with most of the pulsar and FRB measurements. In the future, when more redshifts and scattering times are available, we will explore the usage of an alternative prior for $A_\tau \widetilde{F} G$, such as a log-normal distribution.

Figure 14 shows the posterior PDFs for the three estimators applied to the nine FRBs with available redshifts (again excluding the nearby FRB 20200120E) and scattering times and using $f_{\mathrm{igm}} = 0.85$, a choice that is discussed below. Scattering is constraining on the redshift if $\hat{z}_{\mathrm{DM},\tau}$ is substantially smaller than $\hat{z}_{\mathrm{DM}}$ or equivalently if $\widehat{\mathrm{DM}}_{\mathrm{h}}(\tau)$ is substantially larger than an a priori chosen value. The scattering-based redshift estimator is likely more accurate for cases where the resulting change in $\widehat{\mathrm{DM}}_{\mathrm{igm}}$ from a scattering-based estimate of DM_{h} is larger than one standard deviation from cosmic fluctuations, or $\widehat{\mathrm{DM}}_{\mathrm{h}}(\tau) > (1+z_{\mathrm{h}})\sigma_{\mathrm{DM_{igm}}}(z_{\mathrm{h}})$.

Applying this constraint using Equations (2), (3), and (23) and approximating $\tilde{r}_1(z_{\mathrm{h}}) \sim z_{\mathrm{h}}$ for redshifts $z_{\mathrm{h}} \lesssim 1$, the criterion for when scattering influences redshift estimates is

$$\tau_{1\ \mathrm{GHz}} \gtrsim 2\ \mathrm{ms} \times A_\tau \widetilde{F} G (f_{\mathrm{igm}}/0.85) z_{\mathrm{h}}. \qquad (28)$$

This expression is consistent with the posterior PDFs shown in Figure 14 for FRBs with different redshifts and scattering times. Those with small scattering times yield nearly identical PDFs for the DM-only and DM+scattering estimators while those with scattering times greater than about 1 ms are clearly influenced by scattering. This unsurprising result simply underscores the consistency of the method.

Table 3 gives redshift estimates for the objects in Table 1. The columns are the FRB name, measured DM, redshift, median host-galaxy DM_{h}, scattering quantity $A_\tau \widetilde{F} G$, and median redshift estimates and credible ranges using narrow and wide ranges for $A_\tau \widetilde{F} G$. Estimates for $A_\tau \widetilde{F} G$ are made by inversion of Equation (11) (again with ν in GHz and τ in ms):

$$A_\tau \widetilde{F} G = 2.1\ (\mathrm{pc}^2\ \mathrm{km})^{-1/3} \times \frac{\nu^4(1+z_{\mathrm{h}})^3\tau(\nu)}{(\mathrm{DM}_{\mathrm{h}}/100\ \mathrm{pc\ cm^{-3}})^2}. \qquad (29)$$

The five FRBs with scattering upper limits yield upper limits on $A_\tau \widetilde{F} G$. The upper limit on $A_\tau \widetilde{F} G$ for FRB 20200120E is very small, consistent with the absence of scattering from either the halo of M81 or the halo of the MW. The values and upper limits on $A_\tau \widetilde{F} G$ are all consistent with the adopted prior that is flat between 0.01 and $10\,(\mathrm{pc}^2\ \mathrm{km})^{-1/3}$.

For the four cases with $\tau \geqslant 3.1$ ms (at 1 GHz), the true redshift is below that of the DM-based estimator and more consistent with the scattering-based estimator using the broader range of $A_\tau \widetilde{F} G$. For small scattering times, $\tau \lesssim 0.1$ ms, the three estimators give the same result because the measured scattering does not require a large DM_{h} for either of the ranges for $A_\tau \widetilde{F} G$. The intermediate cases FRB 20191001A and FRB 20180924A with $\tau = 1.5$ ms and 1.8 ms, respectively, are mixed, with the former object being more consistent with the scattering-based redshift and the latter slightly more consistent with the DM-only estimator. The outlier in this sample of nine is FRB 20190611B, where the true redshift is larger than the mode, mean, or median of any of the estimators but is not improbable for the DM-only estimator or the scattering estimator with a broad range of $A_\tau \widetilde{F} G$. Macquart et al. (2020) noted that the association of the FRB with the galaxy at $z = 0.378$ is tentative, and the redshift estimations here may reflect that possibility.

5.3. Constraints on the Baryon Fraction f_{igm}

Figure 15 shows $\hat{z}$ plotted against z using the three different redshift estimators with values of 0.4 and 0.8 for f_{igm} that allow comparison with two of the panels in Figure 12. The plotted points are the median values of the posterior PDFs. Note that here the posterior PDF for DM_{h} is calculated only for the 9 objects with τ measurements compared to the 13 objects used in Figures 12 and 13. The other two estimators incorporate scattering using the two different ranges for $A_\tau \widetilde{F} G$ described

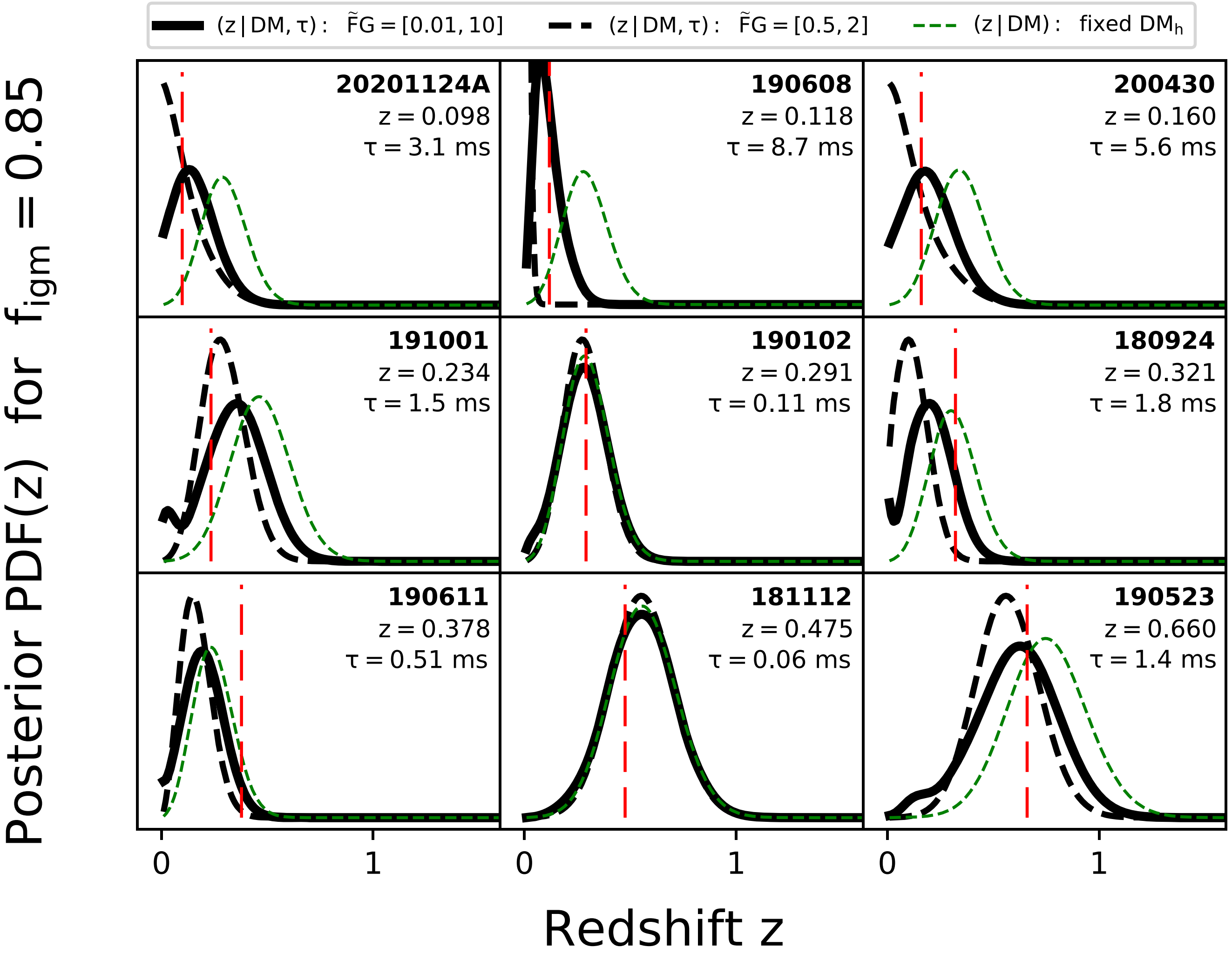

Figure 14. Posterior redshift PDFs for three different redshift estimators applied to nine FRBs with both redshift and scattering measurements and using an ionized baryonic fraction $f_{\rm igm} = 0.85$. Two (solid and dashed black lines) use the measured DM along with the scattering time τ but with different ranges for $A_\tau \widetilde{F}G$. The third (green dashed line) uses only the measured DM. In each panel, the red dashed vertical line indicates the measured redshift of the associated host galaxy. In each panel, the redshift and scattering time at 1 GHz are also given.

above The larger value $f_{\rm igm} = 0.8$ yields much greater consistency between $\hat{z}$ and z than the smaller value.

To identify the plausible range for $f_{\rm igm}$, we show the mean and rms residual $\langle \delta z\rangle = \langle \hat{z} - z\rangle$ and $\sigma_{\delta\hat{z}} = \langle (\delta z)^2\rangle^{1/2}$ for the three estimators in the left- and right-hand panels of Figure 16. The figure shows $\langle \delta z\rangle$ to be monotonically decreasing with larger $f_{\rm igm}$ for all three estimators and $\sigma_{\delta\hat{z}}$ decreasing to $f_{\rm igm} \sim 0.85 \pm 0.05$. It is notable that all three of the redshift estimators are better for larger values of the baryonic fraction, $f_{\rm igm} \gtrsim 0.8$, showing less bias and less scatter about the measured redshifts.

The DM-based estimator remains positive for values of $f_{\rm igm} \lesssim 1$ and is therefore biased. The wide-range $A_\tau \widetilde{F}G$ scattering estimator crosses zero at $f_{\rm igm} \sim 0.85$, and the narrow-range estimator crosses at $f_{\rm igm} \sim 0.75$. The rms residual curve for the DM-only estimator decreases monotonically and is slightly below that of the narrow-$A_\tau \widetilde{F}G$ estimator at $f_{\rm igm} = 1$ but is larger than both scattering-based estimators for $f_{\rm igm} \lesssim 0.85$. The two scattering-based estimators bottom out at $f_{\rm igm} \simeq 0.8$ to 0.9. Considering both the bias and the minimum rms residual, a value $f_{\rm igm} \simeq 0.8$ to 0.9 appears to give the best match. For these values, the bias of the wide-$A_\tau \widetilde{F}G$ scattering estimator is $|\langle \delta\hat{z}\rangle| \lesssim 0.02$ and the rms redshift error is $\sigma_{\delta\hat{z}} \sim 0.1$.

5.4. Discussion of Individual FRBs with Measured Scattering Times

In previous sections, scattering has been attributed to host galaxies, yielding a range for $A_\tau \widetilde{F}G$ of $\sim [0.1, 9]\,{\rm pc\,cm^{-3}}$ (Table 3), from which estimates for the host-galaxy DM contribution and redshift were made. We now discuss individually each FRB for which there are both scattering and redshift measurements. Quoted scattering times are referenced to 1 GHz.

FRB 20180924A ($\tau = 1.78 \pm 0.08$ ms, $z = 0.321$): Heintz et al. (2020, hereafter H20) designate the galaxy association as high probability (A class); the FRB is only slightly offset from the galaxy center. Scattering is constraining on the redshift for smaller values of the baryon fraction, $f_{\rm igm} \lesssim 0.6$, but the DM-only estimate matches the measured redshift for $f_{\rm igm} \gtrsim 0.7$. For these larger $f_{\rm igm}$, $A_\tau \widetilde{F}G \simeq 8.7$ is needed to better match the redshift.

FRB 20181112A ($\tau = 0.06 \pm 0.003$ ms, $z = 0.475$): Also designated a high-probability association by H20. The

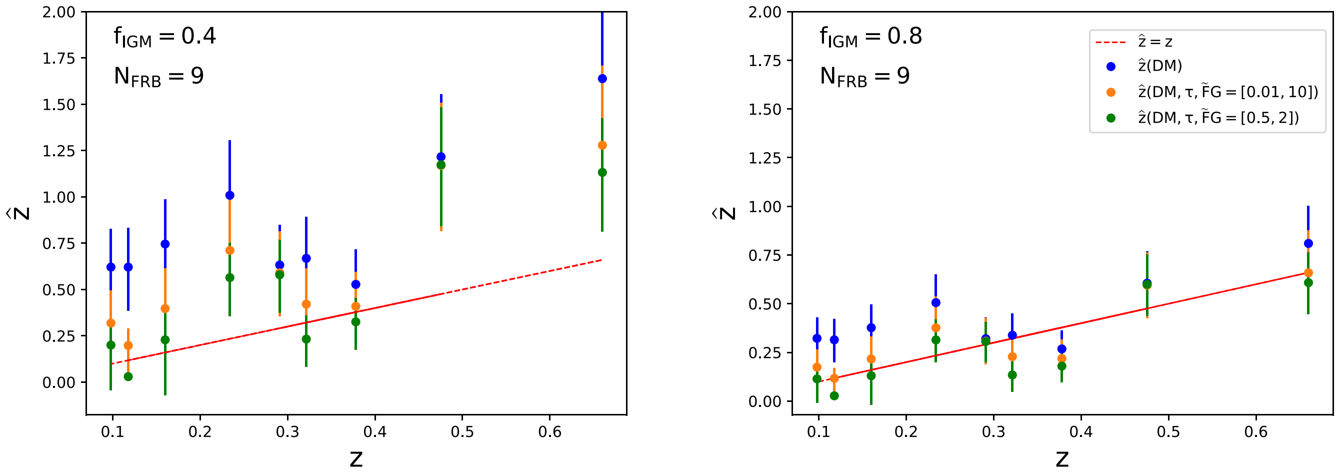

Figure 15. Redshift estimates vs. true redshift for nine FRB cases where redshifts and scattering measurements are both available. Left: $f_{\rm igm} = 0.4$; right: $f_{\rm igm} = 0.8$. Vertical bars represent the 68% credible region centered on the median value derived from the posterior PDFs. The red lines show $\hat{z} = z$. The legend applies to both frames.

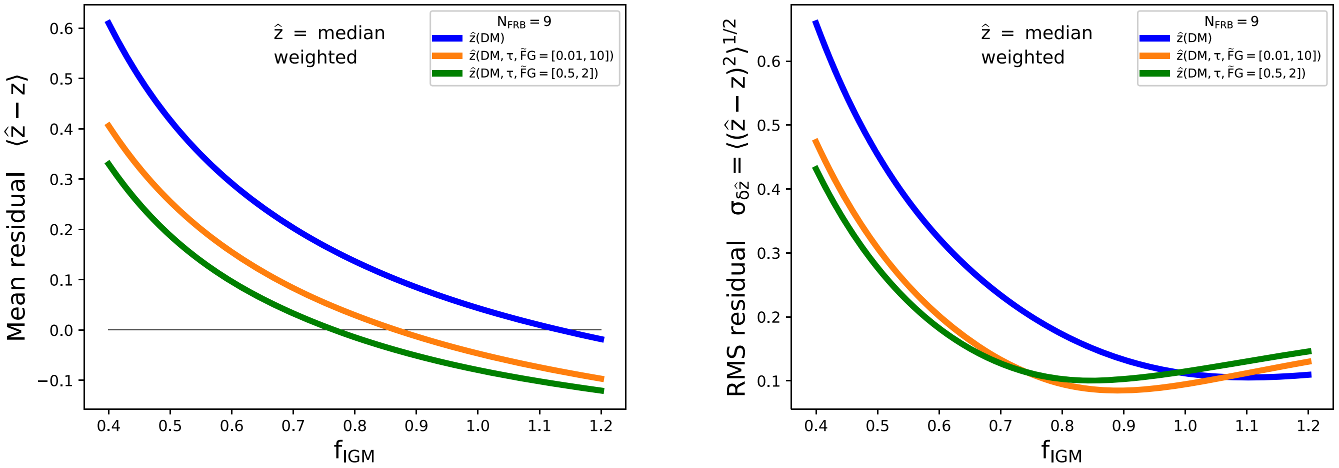

Figure 16. Mean (top) and rms (bottom) residual difference between estimated and true redshifts vs. $f_{\rm igm}$. Redshift estimates are median values calculated from posterior PDFs for $\hat{z}$. The three curves for each set correspond to $\hat{z}$ estimators using DM only and two using the combined DM and τ estimator with a wide or narrow range of $\widetilde{F}G$, as indicated in the legend.

scattering is too small to be constraining, in accordance with the criterion in Equation (28). The measured redshift is slightly less than the median $\hat{z}$ for all three estimators.

FRB 20190102B ($\tau = 0.11 \pm 0.008$ ms, $z = 0.291$): Another high-probability association (H20). Scattering is too small to be constraining. The $\hat{z}$ estimators favor $f_{\rm igm} \gtrsim 0.6$.

FRB 20190523A ($\tau = 1.4 \pm 0.2$ ms, $z = 0.66$): The FRB is offset from the galaxy center by 27 kpc, and there is a 7% probability of a chance association, yielding a C classification by H20. Scattering is constraining and requires $A_\tau \widetilde{F} G \sim 2$ in order to match the measured redshift for $f_{\rm igm} = 0.85$. The DM-only estimator requires $f_{\rm igm} \gtrsim 0.6$.

Given the large offset from the galaxy center, it is possible that the required value of $A_\tau \widetilde{F} G$ receives a significant contribution from a geometric factor, $G > 1$. This could arise from a contribution to the DM from a galaxy halo or disk with a very small value of $\widetilde{F}$ but with a large geometric boost. An alternative is that the candidate galaxy association is incorrect. Given that the galaxy has the largest redshift in the sample, a misassociation would require reassessment of the empirical DM(z) statistics.

FRB 20190608B ($\tau = 8.7 \pm 0.5$ ms, $z = 0.118$): An A-class association with the FRB coincident in projection with a spiral arm (H20; see also Macquart et al. 2020; Mannings et al. 2021). Scattering is strongly constraining on redshift and requires smaller values of $A_\tau \widetilde{F} G$ in the [0.1, 10] range. The DM-only estimate is a poor match for all values of $f_{\rm igm}$.

FRB 20190611B ($\tau = 0.51 \pm 0.06$ ms, $z = 0.378$): The FRB–galaxy association was called "tentative" by Macquart et al. (2020) but designated as class A by H20 in spite of a significant offset ∼11 ± 4 kpc from the galaxy center compared to an *i*-band radial size of ∼2 kpc.

The galaxy's redshift is within the credible region for $\hat{z}$ only for relatively small values of $f_{\rm igm} \lesssim 0.7$ for the DM-only estimator and for $f_{\rm igm} \lesssim 0.6$ and $\lesssim 0.5$ using the DM–τ estimators with wide and narrow ranges of $A_\tau \widetilde{F} G$, respectively. This implies that a smaller than normal IGM contribution to the DM is needed to match the DM inventory and allow the host-galaxy $\rm DM_h$ to be large enough to account for the measured scattering for the two ranges of $A_\tau \widetilde{F} G$ considered in the analysis.

From Table 2, the median $\rm DM_{igm}$ using the the log-normal model of Section 2.2 is 320 pc cm^{-3}, nearly equal to the measured $\mathrm{DM} = 321\ \mathrm{pc\ cm^{-3}}$ without any consideration of contributions from the MW or host galaxy. When those contributions are included, the measured DM is estimated to have a total extragalactic contribution, $\mathrm{DM_{xg}} \simeq \mathrm{DM_{igm}} + \mathrm{DM_h}/(1+z_h) = 211 \pm 17\ \mathrm{pc\ cm^{-3}}$ and an implied IGM contribution, $\mathrm{DM_{igm}} = \mathrm{DM_{xg}} - \mathrm{DM_h}/(1+z_h) \simeq 179\ \mathrm{pc\ cm^{-3}}$, with an uncertainty of about $40\ \mathrm{pc\ cm^{-3}}$ (where we have used the geometric mean of the asymmetric confidence interval values for $\mathrm{DM_h}$ in quadrature with the uncertainty in the MW contribution).

This IGM value is $\sim$141 $\mathrm{pc\ cm^{-3}}$ below the median IGM from the log-normal model of Section 2.2, or about 1.5 times the 68% confidence range, $\sigma_- = 97\ \mathrm{pc\ cm^{-3}}$, to smaller $\mathrm{DM_{igm}}$ values (column 7 of Table 2). While this is not overly improbable in a nine-object sample, the necessarily smaller IGM contribution implies that the LoS to this FRB needs further study.

The measured scattering requires the second largest value of $A_\tau \widetilde{F} G$ given in Table 3 (column 3), which is based on $f_{\mathrm{igm}} = 0.85$, a value that is consistent with the entire set of objects. Using Equation (29) along with the median inferred value for $\mathrm{DM_h} = 58\ \mathrm{pc\ cm^{-3}}$, we require $A_\tau \widetilde{F} G \simeq 8.3$ (Table 3).

The summary for this source is that the DM inventory requires a lower-than average contribution from the IGM for the redshift of the proposed galaxy association. However, it is not so extreme that the association is necessarily incorrect. However an incorrect association is certainly a possibility.

FRB 20191001A ($\tau = 1.5 \pm 0.1$, $z = 0.234$): An A-class association (H20) with a 2:1 offset relative to the i-band radial size but with the FRB overlying a spiral arm (Mannings et al. 2021). The redshift is overestimated by the DM-only estimator but is consistent with either of the scattering-based estimators.

FRB 20200430A ($\tau = 5.6 \pm 2.8$ ms, $z = 0.160$): An A-class association (H20). Scattering is constraining on the redshift. The DM-only redshift estimator is disfavored compared to the DM–τ estimators, especially for smaller values of $f_{\mathrm{igm}} \lesssim 0.6$. But even for $f_{\mathrm{igm}} \geqslant 0.9$, the scattering constraint gives a better estimate.

FRB 20201124A ($\tau = 3.13 \pm 1.7$ ms, $z = 0.098$): The lowest-redshift galaxy in the sample, J0508+2603, has a stellar mass comparable to the two candidate galaxies for FRB 20190523A and FRB 20191001A (Ravi et al. 2022, H20) with an extended source spatially coincident with the FRB and associated with star formation activity. The scattering time is large enough to constrain the redshift with both DM–τ estimates yielding credible values superior to the DM-only result for any value of f_{igm}. The two DM–τ estimates are equally good for $f_{\mathrm{igm}} \gtrsim 0.7$.

In summary, combined measurements of the scattering time τ and DM yield better estimates for redshift than DM-only estimates in the majority of the nine FRBs for which such measurements exist along with redshifts. The exceptions are when the scattering time is too small to constrain the host-galaxy DM using plausible values of the fluctuation-geometry parameter $A_\tau \widetilde{F} G$.

5.5. FRBs with Scattering Upper Limits

Four FRBs in Table 1 have A-class galaxy associations (H20). Three of these (FRBs 20121102A, 20180916B, and 20190711A) have scattering upper limits too large to be constraining on the host-galaxy DM or on the redshift. The fourth case, FRB 20200120E, has a very low upper limit that is informative about scattering in the halos of the MW and M81, as previously mentioned. A detailed interpretation of that case is deferred to another paper (in preparation).

FRB 20121102A warrants additional discussion because Balmer-line measurements place ancillary constraints on $\mathrm{DM_h}$ (Tendulkar et al. 2017). FRB 20121102A is in a dwarf, star-forming galaxy at redshift $z_h = 0.193$ and produces bursts with a total $\mathrm{DM} \approx 570\ \mathrm{pc\ cm^{-3}}$ contributed to roughly equally by the MW, the IGM, and its dwarf host galaxy (Bassa et al. 2017; Kokubo et al. 2017; Tendulkar et al. 2017). Intensity scintillations imply a small Galactic contribution to temporal broadening ($\sim$20 μs at 1 GHz), and an upper bound on extragalactic scattering is $\tau(1\ \mathrm{GHz}) < 0.6$ ms. The dependencies of $\mathrm{DM_h}$ and extragalactic scattering on redshift and other quantities shown in Figure 9 (left panel) indicate that the upper bound on τ is consistent with the plausible range of $\mathrm{DM_h}$ (see Figure 2) combined with possible values for $A_\tau \widetilde{F} G$ that match the ranges for $A_\tau \widetilde{F} G$ implied by FRBs with measured τ and with the expectations based on Galactic pulsars.

6. Summary and Conclusions

We have used dispersion and scattering measurements on FRBs with candidate host-galaxy associations and their redshifts to characterize scattering. We have shown in Section 5.2 that the combined DM–τ redshift estimator more accurately predicts the redshift than a DM-only-based estimate. Overall, the results are consistent with our assumption that scattering of FRBs is dominated by galaxy disks, including that of the MW, but is not significant from galaxy halos or the IGM. It is possible that some halos will produce significant scattering if feedback processes can drive small-scale density fluctuations. These may occur at higher redshifts ($\gtrsim$1) than in the sample discussed here (Ocker et al. 2022b).

We have derived an expression (Equation (23)) for the host-galaxy DM, $\mathrm{DM_h} \propto (1+z)^{3/2}(\tau/A_\tau \widetilde{F} G)^{1/2}$, in terms of the scattering time τ and turbulence fluctuation parameter $\widetilde{F}$. This is useful by itself for providing an order-of-magnitude estimate where the (considerable) uncertainty derives primarily from that for $\widetilde{F}$. When combined with a model for the IGM's contribution to the DM inventory, the expression for $\mathrm{DM_h}$ also provides the basis for a scattering- (and dispersion-) based redshift estimate. The scattering time is constraining on the redshift if it satisfies the inequality given in Equation (28) and a specific range of values for the composite scattering quantity $A_\tau \widetilde{F} G$ is known or assumed. Similarly, if independent constraints on the host galaxy's $\mathrm{DM_h}$ are known from (for example) emission-line measurements, then $A_\tau \widetilde{F} G$ can be estimated using Equation (29).

Imperfections in this method are also tied to the question of whether some of the candidate FRB–galaxy associations are genuine. Two of the FRBs (FRB 20190523A and FRB 20190611B) are offset significantly from their proposed galaxy associations. If the associations are real, significant contributions to DM and to scattering must come from the outskirts of the galaxies or from their halos. That is in contrast to the MW and raises the caveat that the large offsets may cast doubt on the reality of those associations.

As discussed in Section 5.4, the redshift of 0.378 for FRB 20190611B is larger than all three of the propagation-based redshift estimates, whereas more typically the DM-based redshift overestimates the redshift. This suggests that the host galaxy might be closer than $z = 0.378$ and would necessarily be much dimmer to avoid identification in the images from Macquart et al. (2020) and Heintz et al. (2020).

FRB 20190523A has the largest redshift (0.66) in the sample that is not inconsistent with the DM- or scattering-based redshift estimates. It requires a large extragalactic contribution $\mathrm{DM}_{\mathrm{xg}} \sim 740\,\mathrm{pc\,cm}^{-3}$, of which about 20% is from the host galaxy at the stated redshift (see Table 2). However, as noted above, the galaxy association (Ravi et al. 2019) is in the C class defined by H20, so conclusions about the source of the large DM may be premature at this point.

We conclude that FRB studies can benefit from redshift estimation that incorporates scattering measurements. This is true especially now when optically determined redshifts are few in number. But we expect it will also help in the future even when more precise redshifts are measured for some but certainly not all FRBs. For this to be the case, scattering measurements need to be robustly differentiated from the frequency–time structure in FRBs that differs from that produced by scattering in either a host galaxy or the MW.

J.M.C., S.K.O., and S.C. acknowledge support from the National Science Foundation (NSF AAG-1815242) and are members of the NANOGrav Physics Frontiers Center, which is supported by the NSF award PHY-2020265. This work was also supported by NASA grant 80NSSC20K0784.

Appendix
Pulse Broadening for the Cloudlet Model

We describe electron-density fluctuations inside a turbulent cloud with a power-law spectrum $\propto C_n^2 q^{-\beta} \exp[-(2\pi q/l_{\mathrm{i}})^2]$ for wavenumbers $2\pi/l_{\mathrm{o}} \leqslant q \lesssim 2\pi/l_{\mathrm{i}}$, where l_{o} and $l_{\mathrm{i}} \ll l_{\mathrm{o}}$ are the outer and inner scales, respectively. We use a Kolmogorov spectrum with $\beta = 11/3$ as a reference spectrum. This builds upon the model originally presented in Cordes et al. (1991).

The integral of the spectrum gives the variance of the electron density inside a cloud, $\sigma_{n_{\mathrm{e}}}^2 = (\varepsilon \bar{n}_{\mathrm{e}})^2 = C_{\mathrm{SM}}^{-1} C_n^2 l_{\mathrm{o}}^{\beta-3}$ with $C_{\mathrm{SM}} = (\beta - 3)/2(2\pi)^{4-\beta}$. We then relate the volume-averaged electron density $n_{\mathrm{e}} = f\bar{n}_{\mathrm{e}}$ to the internal density $\bar{n}_{\mathrm{e}}$ using the filling factor, f, and express the volume-averaged C_n^2 for the Kolmogorov case ($\beta = 11/3$) as

$$C_n^2 = C_{\mathrm{SM}} F n_{\mathrm{e}}^2, \tag{A1}$$

where $C_{\mathrm{SM}} = [3(2\pi)^{1/3}]^{-1}$ and the parameter $F = \zeta\varepsilon^2/f l_{\mathrm{o}}^{2/3}$ characterizes the fluctuation properties of the medium. Different components of the NE2001 model have different values of F.

With these definitions, we relate the scattering time τ to the DM of a medium as follows. In Euclidean space, the mean scattering time is given by the LoS integral

$$\langle \tau \rangle = \frac{1}{2c} \int_0^d ds\, s(1 - s/d)\eta(s), \tag{A2}$$

where $\eta(s)$ is the mean-square scattering angle per unit distance, which may vary along the LoS, and is given at a single location by Cordes & Rickett (1998)

$$\begin{aligned} \eta(s) &= \frac{\Gamma(3 - \beta/2)}{4 - \beta}\left(\frac{2\pi}{l_{\mathrm{i}}}\right)^{4-\beta} \lambda^4 r_{\mathrm{e}}^2 C_n^2(s) \\ &= \Gamma(7/6) r_{\mathrm{e}}^2 \lambda^4 \widetilde{F} n_{\mathrm{e}}^2 \end{aligned} \tag{A3}$$

based on Equation (A1) and using $\beta = 11/3$ for the second equality. The parameter $\widetilde{F}$ in Equation (A3) is

$$\widetilde{F} \equiv F l_{\mathrm{i}}^{-1/3} = \frac{\zeta\varepsilon^2}{f(l_{\mathrm{o}}^2 l_{\mathrm{i}})^{1/3}}. \tag{A4}$$

For a layer of thickness L with constant density and constant F, the DM is $\mathrm{DM}_\ell = n_{\mathrm{e}} L$, and the mean scattering time becomes

$$\langle \tau \rangle = C_\tau \nu^{-4} \widetilde{F} \mathrm{DM}_\ell^2 (1 - 2L/3d) G, \tag{A5}$$

where $C_\tau = \Gamma(7/6) c^3 r_{\mathrm{e}}^2/4$ is a constant that depends only weakly on any modification from the $\beta = 11/3$ spectrum.

The last consideration is how scattering times estimated from pulse or burst shapes are related to the mean scattering time $\langle\tau\rangle$. The scattered shape for an emitted narrow impulse is the pulse-broadening function (PBF), often assumed to be a one-sided exponential, $p(t) = \tau_e^{-1}\exp(-t/\tau_e)\Theta(t)$, where Θ is the Heaviside function. The scattering time is typically estimated by comparing the measured pulse shape with the convolution of $p(t)$ with an assumed intrinsic pulse shape to determine a best-fit value. In this case, the mean scattering time is identical to the e^{-1} time. However, scattering from a power-law wavenumber spectrum can show PBFs with much longer tails than an exponential (e.g., Lambert & Rickett 1999), yielding $\langle\tau\rangle > \tau_e$ by an amount that depends on details of the wavenumber spectrum (the inner scale, the spectral index β, and the amplitude C_n^2). To account for how empirical estimates for the scattering time are related more closely to the e^{-1} time than to the mean, we define a factor $A_\tau \equiv \tau_e/\langle\tau\rangle \leqslant 1$. Assuming also that the scattering region is thin, $L/d \ll 1$, we write the measured τ as (dropping the "e" subscript)

$$\tau \simeq A_\tau C_\tau \nu^{-4} \widetilde{F} \mathrm{DM}_\ell^2 G. \tag{A6}$$

The factor A_τ depends on the ratio, $l_{\mathrm{i}}/l_{\mathrm{d}}$, of the inner scale to the diffraction scale, where the latter is related to the characteristic scattering angle and thus to the width of the PBF. When the ratio is small, $l_{\mathrm{i}}/l_{\mathrm{d}} \ll 0.1$, $A_\tau \sim 1/6$ for a Kolmogorov spectrum with $\beta = 11/3$ but increases to $A_\tau \sim 0.7$ for $l_{\mathrm{i}}/l_{\mathrm{d}} = 1$. For a fixed inner scale, $l_{\mathrm{i}}/l_{\mathrm{d}}$ is larger for stronger scattering and $A_\tau \to 1$ (unpublished notes by JMC). For FRBs that show significant scattering as pulse broadening, it is likely that A_τ is close to unity. Because of its model dependence, we simply include A_τ in Equation (A6) as one of the factors in the lumped quantity, $A_\tau \widetilde{F} G$.

ORCID iDs

J. M. Cordes https://orcid.org/0000-0002-4049-1882
Stella Koch Ocker https://orcid.org/0000-0002-4941-5333
Shami Chatterjee https://orcid.org/0000-0002-2878-1502

References

Amiri, M., Andersen, B. C., Bandura, K., et al. 2021, ApJS, 257, 59
Arcus, W. R., Macquart, J. P., Sammons, M. W., James, C. W., & Ekers, R. D. 2021, MNRAS, 501, 5319

Bannister, K. W., Deller, A. T., Phillips, C., et al. 2019, Sci, 365, 565

Bassa, C. G., Tendulkar, S. P., Adams, E. A. K., et al. 2017, ApJL, 843, L8

Bhandari, S., Bannister, K. W., Lenc, E., et al. 2020, ApJL, 901, L20

Bhandari, S., Kumar, P., Shannon, R. M., & Macquart, J. P. 2019, ATel, 12940, 1

Bhardwaj, M., Gaensler, B. M., Kaspi, V. M., et al. 2021, ApJL, 910, L18

Bhat, N. D. R., Cordes, J. M., Camilo, F., Nice, D. J., & Lorimer, D. R. 2004, ApJ, 605, 759

Brisken, W. F., Macquart, J.-P., Gao, J. J., et al. 2010, ApJ, 708, 232

Cassanelli, T., Leung, C., Rahman, M., et al. 2022, AJ, 163, 65

Chawla, P., Andersen, B. C., Bhardwaj, M., et al. 2020, ApJL, 896, L41

CHIME/FRB Collaboration, Andersen, B. C., Bandura, K., et al. 2019, ApJL, 885, L24

Cho, H., Macquart, J.-P., Shannon, R. M., et al. 2020, ApJL, 891, L38

Cordes, J. M., & Chatterjee, S. 2019, ARA&A, 57, 417

Cordes, J. M., & Lazio, T. J. W. 2001, ApJ, 549, 997

Cordes, J. M., & Lazio, T. J. W. 2002, arXiv:astro-ph/0207156

Cordes, J. M., & Rickett, B. J. 1998, ApJ, 507, 846

Cordes, J. M., Weisberg, J. M., Frail, D. A., Spangler, S. R., & Ryan, M. 1991, Natur, 354, 121

Cordes, J. M., Wharton, R. S., Spitler, L. G., Chatterjee, S., & Wasserman, I. 2016, arXiv:1605.05890

Day, C. K., Deller, A. T., Shannon, R. M., et al. 2020, MNRAS, 497, 3335

Deller, A. T., Goss, W. M., Brisken, W. F., et al. 2019, ApJ, 875, 100

Dolag, K., Gaensler, B. M., Beck, A. M., & Beck, M. C. 2015, MNRAS, 451, 4277

Fonseca, E., Andersen, B. C., Bhardwaj, M., et al. 2020, ApJL, 891, L6

Gajjar, V., Siemion, A. P. V., Price, D. C., et al. 2018, ApJ, 863, 2

Goldstein, M. L., Wicks, R. T., Perri, S., & Sahraoui, F. 2015, RSPTA, 373, 20140147

Hallinan, G., Ravi, V., Weinreb, S., et al. 2019, BAAS, 51, 255

Heintz, K. E., Prochaska, J. X., Simha, S., et al. 2020, ApJ, 903, 152

Hessels, J. W. T., Spitler, L. G., Seymour, A. D., et al. 2019, ApJL, 876, L23

Hill, J. C., Ferraro, S., Battaglia, N., Liu, J., & Spergel, D. N. 2016, PhRvL, 117, 051301

Inoue, S. 2004, MNRAS, 348, 999

Ioka, K. 2003, ApJL, 598, L79

James, C. W., Prochaska, J. X., Macquart, J.-P., et al. 2022, MNRAS, 509, 4775

Josephy, A., Chawla, P., Fonseca, E., et al. 2019, ApJL, 882, L18

Keating, L. C., & Pen, U.-L. 2020, MNRAS, 496, L106

Kilpatrick, C. D., Fong, W., Prochaska, J. X., et al. 2021, ATel, 14516, 1

Kirsten, F., Marcote, B., Nimmo, K., et al. 2022, Natur, 602, 585

Kokubo, M., Mitsuda, K., Sugai, H., et al. 2017, ApJ, 844, 95

Krishnakumar, M. A., Mitra, D., Naidu, A., et al. 2015, ApJ, 804, 23

Kumar, P., Day, C. K., Shannon, R. M., et al. 2020, ATel, 13694, 1

Kumar, P., Shannon, R. M., Moss, V., Qiu, H., & Bhandari, S. 2021, ATel, 14502, 1

Kusiak, A., Bolliet, B., Ferraro, S., et al. 2021, PhRvD, 104, 043518

Lambert, H. C., & Rickett, B. J. 1999, ApJ, 517, 299

Leung, C., Mena-Parra, J., Masui, K., et al. 2021, AJ, 161, 81

Luan, J., & Goldreich, P. 2014, ApJL, 785, L26

Macquart, J.-P., & Koay, J. Y. 2013, ApJ, 776, 125

Macquart, J. P., Prochaska, J. X., McQuinn, M., et al. 2020, Natur, 581, 391

Mannings, A. G., Fong, W.-F., Simha, S., et al. 2021, ApJ, 917, 75

Marcote, B., Nimmo, K., Hessels, J. W. T., et al. 2020, Natur, 577, 190

Masui, K., Lin, H.-H., Sievers, J., et al. 2015, Natur, 528, 523

McQuinn, M. 2014, ApJL, 780, L33

Nimmo, K., Hessels, J. W. T., Kirsten, F., et al. 2022, NatAs, 6, 393

Niu, C.-H., Aggarwal, K., Li, D., et al. 2021, Natur, in press, arXiv:2110.07418

Ocker, S. K., Cordes, J. M., & Chatterjee, S. 2020, ApJ, 897, 124

Ocker, S. K., Cordes, J. M., & Chatterjee, S. 2021, ApJ, 911, 102

Ocker, S. K., Cordes, J. M., Chatterjee, S., et al. 2022a, ApJ, 931, 87

Ocker, S. K., Cordes, J. M., Chatterjee, S., et al. 2022b, arXiv:2203.16716

Pastor-Marazuela, I., Connor, L., van Leeuwen, J., et al. 2021, Natur, 596, 505

Pol, N., Lam, M. T., McLaughlin, M. A., Lazio, T. J. W., & Cordes, J. M. 2019, ApJ, 886, 135

Prochaska, J. X., Macquart, J.-P., McQuinn, M., et al. 2019, Sci, 366, 231

Prochaska, J. X., & Neeleman, M. 2018, MNRAS, 474, 318

Prochaska, J. X., & Zheng, Y. 2019, MNRAS, 485, 648

Qiu, H., Shannon, R. M., Farah, W., et al. 2020, MNRAS, 497, 1382

Ramachandran, R., Mitra, D., Deshpande, A. A., McConnell, D. M., & Ables, J. G. 1997, MNRAS, 290, 260

Ravi, V., Catha, M., D'Addario, L., et al. 2019, Natur, 572, 352

Ravi, V., Law, C. J., Li, D., et al. 2022, MNRAS, 513, 982

Rickett, B., Johnston, S., Tomlinson, T., & Reynolds, J. 2009, MNRAS, 395, 1391

Rickett, B. J. 1990, ARA&A, 28, 561

Scheuer, P. A. G. 1968, Natur, 218, 920

Shull, J. M., & Danforth, C. W. 2018, ApJL, 852, L11

Shull, J. M., Smith, B. D., & Danforth, C. W. 2012, ApJ, 759, 23

Simard, D., & Ravi, V. 2021, arXiv:2107.11334

Smercina, A., Bell, E. F., Price, P. A., et al. 2020, ApJ, 905, 60

Spangler, S. R., & Gwinn, C. R. 1990, ApJL, 353, L29

Taylor, J. H., & Cordes, J. M. 1993, ApJ, 411, 674

Tendulkar, S. P., Bassa, C. G., Cordes, J. M., et al. 2017, ApJL, 834, L7

The CHIME/FRB Collaboration, Andersen, B. C., Bandura, K., et al. 2021, arXiv:2107.08463

Vedantham, H. K., & Phinney, E. S. 2019, MNRAS, 483, 971

Yamasaki, S., & Totani, T. 2020, ApJ, 888, 105

Yao, J. M., Manchester, R. N., & Wang, N. 2017, ApJ, 835, 29

Zhang, B. 2018, ApJL, 867, L21